J. Fluid Mech. (2024), *vol*. 990, A2, doi:10.1017/jfm.2024.508

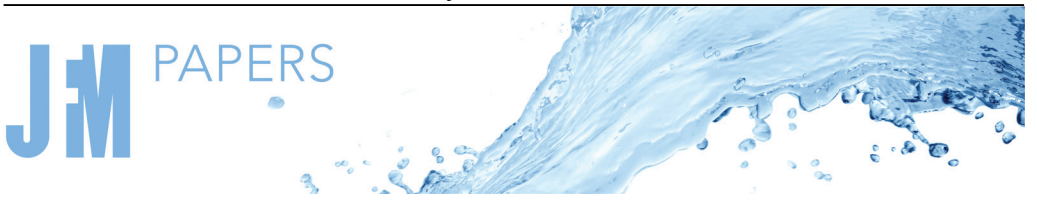

Turbulence modulation by charged inertial particles in channel flow

Yuankai Cui[1], **Huan Zhang**[1],† **and Xiaojing Zheng**[2]

[1]Center for Particle-laden Turbulence, Lanzhou University, Lanzhou 730000, PR China

[2]Research Center for Applied Mechanics, Xidian University, Xi'an 710071, PR China

(Received 7 November 2023; revised 7 May 2024; accepted 19 May 2024)

Large amounts of small inertial particles embedded in a turbulent flow are known to modify the turbulent statistics and structures, a phenomenon referred to as turbulence modulation. While particle electrification is ubiquitous in particle-laden turbulence and significantly alters particle behaviour, the effects of inter-particle electrostatic forces on turbulence modulation and the underlying physical mechanisms remain unclear. To fill this gap, we perform a series of point-particle direct numerical simulations of turbulent channel flows at a friction Reynolds number of approximately 540, laden with uncharged and charged bidisperse particles. The results demonstrate that, compared to flows laden with uncharged particles, the presence of inter-particle electrostatic forces leads to substantial changes in both turbulent intensities and structures. In particular, the inner-scaled mean streamwise fluid velocity is found to shift towards lower values, indicating a noticeable increase in fluid friction velocity. Turbulent intensities appear to be further suppressed through facilitating the particles to extract momentum from the fluid phase and increasing extra turbulent kinetic dissipation by particles. Importantly, the overall drag is enhanced by indirectly strengthening the contribution of particle stress, even though the contribution of the total fluid stress is decreased. On the other hand, the magnitude of the large-scale motions is weakened by simultaneously reducing turbulent production and increasing particle feedback around the scales of the large-scale motions. Meanwhile, the average streaky fluid structures in the streamwise–spanwise planes and inclined fluid structures in the streamwise–wall-normal planes become expanded and flattened, respectively.

Key words: particle/fluid flow

1. Introduction

Particle-laden turbulent flows consist of massive disperse particles embedded in a turbulent flow. Due to triboelectric charging and other electrification mechanisms,

† Email address for correspondence: zhanghuan@lzu.edu.cn

particles tend to become highly charged, and the electrostatic forces exerted on the particles are typically comparable to their gravitational forces (Lacks & Sankaran 2011; Zheng 2013). This electrical effect is common in various natural phenomena and industrial applications, such as wind-blown sand movements (Zheng, Huang & Zhou 2003), dust storms (Zhang & Zhou 2020, 2023; Zhang, Tan & Zheng 2023*b*), fluidized beds (Sippola *et al.* 2018) and pneumatic conveying of powders (Owen 1969; Schwindt *et al.* 2017).

It has been recognized that inter-particle electrostatic forces significantly affect the dynamics, distribution and aggregation of particles in turbulent flows and therefore cannot be neglected. In this context, many early studies were concerned with homogeneous isotropic turbulence. Pioneering theoretical work by Alipchenkov, Zaichik & Petrov (2004) established a statistical model for describing like-charged particles in homogeneous isotropic turbulence, which is based on the kinetic equation for the probability density distribution of relative velocity between a pair of particles. The model predicted that particle clustering was considerably suppressed in the presence of inter-particle electrostatic interactions. This phenomenon is verified later by the laboratory holographic measurement (Lu *et al.* 2010) and direct numerical simulations (Karnik & Shrimpton 2012; Lu & Shaw 2015; Di Renzo & Urzay 2018; Boutsikakis, Fede & Simonin 2022; Ruan, Gorman & Ni 2024). In addition to homogeneous isotropic turbulence, Grosshans and co-workers conducted a series of direct numerical simulations and large-eddy simulations of charged particles embedded in turbulent channel and turbulent duct flows (e.g. Grosshans & Papalexandris 2016, 2017; Grosshans *et al.* 2021). Their research revealed that the concentration, velocity and flux of the particles were considerably influenced by inter-particle electrostatic forces by a factor of five. More recently, by combining the data from direct numerical simulations and semi-analytical formulations of particle concentrations derived from the kinetic equation for the particle distribution function, we uncovered that the mean concentration of charged particles in turbulent channel flows was determined jointly by three mechanisms: biased sampling, turbophoresis and electrostatic drift (Zhang, Cui & Zheng 2023*a*). The former two mechanisms arise due to biased sampling of fluid flow by particles (i.e. preferential concentration; see Eaton & Fessler 1994; Marchioli & Soldati 2002; Sardina *et al.* 2012) and the non-uniform distribution of turbulent intensity (Caporaloni *et al.* 1975; Reeks 1983). The last mechanism is caused by the inter-particle electrostatic forces, which contributes to an increase or decrease in the particle concentration exceeding one order of magnitude.

Previous studies have demonstrated that the presence of uncharged particles could substantially alter both the turbulent intensity and turbulent structure of the carrier fluid phase. The physical mechanisms responsible for the turbulence modulation contain mainly (1) kinetic energy transfer between the particles and fluid phase, (2) additional dissipation induced by the particles, and (3) the formation of vortex shedding and wakes behind the particles (Balachandar & Eaton 2010). However, the relative importance of these mechanisms varies with the specific flow configurations and depends on various key parameters, including (1) particle size (e.g. Tsuji & Morikawa 1982; Tsuji, Morikawa & Shiomi 1984; Gore & Crowe 1989, 1991; Kulick, Fessler & Eaton 1994; Pan & Banerjee 1996), (2) particle Reynolds number (e.g. Hetsroni 1989; Yu *et al.* 2021), (3) particle Stokes number (e.g. Lee & Lee 2015; Li, Luo & Fan 2016; Wang & Richter 2019*b*), and (4) particle volume fraction and mass loading (e.g. Kulick *et al.* 1994; Li *et al.* 2001; Zhao, Andersson & Gillissen 2013; Picano, Breugem & Brandt 2015; Costa, Brandt & Picano 2021). As a consequence, the modulation of turbulent intensity and turbulent structure appears to be either augmented or attenuated, nonlinearly and non-monotonically depending on the mentioned key particle parameters.

Earlier studies suggested that finer particles tend to suppress turbulent intensity while coarser particles tend to enhance it, but many recent researches have questioned this argument. By integrating a wealth of existing experimental results in various flow configurations, Gore & Crowe (1989) introduced a threshold particle-to-fluid length scale ratio of approximately 0.1, below (beyond) which turbulence attenuation (augmentation) occurs. This length scale ratio is defined as the ratio of particle diameter to the integral length scale of the unladen fluid flow. Although most point-particle direct numerical simulations (PP-DNS) of sub-Kolmogorov-sized particles embedded in homogeneous isotropic and channel turbulence exhibit a turbulence attenuation (e.g. Pan & Banerjee 1996; Li *et al.* 2016; Gao, Samtaney & Richter 2023), some simulations have found turbulence augmentation with sub-Kolmogorov-sized particles (Ahmed & Elghobashi 2000; Kasbaoui 2019). In particular, turbulence attenuation or augmentation appears to depend mainly on the particle Stokes number and mass loading for point-particles (Dave & Kasbaoui 2023). On the other hand, turbulent flows laden with finite-size (large) particles, evaluated by particle-resolved direct numerical simulations (PR-DNS), may experience both attenuation and enhancement (e.g. Pan & Banerjee 1997; Shao, Wu & Yu 2012; Costa *et al.* 2021; Yousefi *et al.* 2023).

By contrast, the dependence of turbulence modulation on other key particle parameters becomes more complex.

First, theoretical considerations by Hetsroni (1989) claimed that when the particle Reynolds number exceeds approximately 400, vortex shedding downstream of the particle occurs, leading to turbulence enhancement. A subsequent numerical and experimental study suggested that vortex shedding would take place at a relatively small particle Reynolds number of 300 (Johnson & Patel 1999). However, due to the presence of particle clusters, vortex shedding is expected to occur at much lower particle Reynolds numbers, which is referred to as cluster-induced turbulence (Capecelatro, Desjardins & Fox 2014, 2015). The opposite effect is observed when the particle Reynolds number is small. Recent PR-DNS of an upward particle-laden turbulent channel by Yu *et al.* (2021) revealed that turbulent intensity decreases throughout the entire channel at low particle Reynolds numbers and increases in the core of the channel, but decreases in the near-wall region at intermediate particle Reynolds numbers, and increases throughout the entire channel at large particle Reynolds numbers.

Second, there is a non-monotonic impact of the particle Stokes number on both turbulent intensity and structure. For instance, Lee & Lee (2015) found that in a turbulent channel, particles with viscous Stokes number 0.5 increase turbulent intensity, while those with viscous Stokes numbers between 5 and 125 reduce it, with the most significant reduction occurring at viscous Stokes number 35. Meanwhile, Wang & Richter (2019*b*) showed that both low- and high-inertia particles appear to strengthen the very-large-scale motions in a turbulent open channel flow at friction Reynolds numbers up to 950, while moderate- and very-high-inertia particles have almost no influence.

Third, turbulence modulation exhibits a more sensitive response to changes in particle volume and mass loading (Elghobashi 1994; Brandt & Coletti 2022). Specifically, when the particle mass loading is very low, the fluid flow remains largely unaffected by the particles, and this regime is termed one-way coupling. When the particle mass loading is high but the volume fraction is small (i.e. dilute dispersion), the fluid flow is noticeably altered by the particles, leading to a two-way coupling regime. When both particle mass loading and volume fraction are sufficiently high (i.e. dense dispersion), inter-particle collisions further arise, and this is termed a four-way coupling regime. Regarding dilute dispersion, Kulick *et al.* (1994) conducted laboratory measurements of turbulent channel

Reference	Geometry	Turbulence augmentation	Turbulence attenuation
Gore & Crowe (1989)	Jet/pipe	$d_p/l_e > 0.1$	$d_p/l_e < 0.1$
Hetsroni (1989)	Jet/pipe	$Re_p > 400$	$Re_p \lesssim 400$
Kulick *et al.* (1994)	VC	—	$d_p/\eta < 1$, $\overline{\phi_m} = 0.2$–0.8
Pan & Banerjee (1996)	HC	$\overline{\phi_m} = 0.0002$, $St^+ \approx 0.22$	$\overline{\phi_m} = 0.0002$, $St^+ \approx 0.06$
Ahmed & Elghobashi (2000)	HSF	$\overline{\phi_m} = 0.1$, $St_\eta \approx 0.23$	$\overline{\phi_m} = 1.0$, $St_\eta = 2.33$
Zhao, Andersson & Gillissen (2010)	HC	—	$\overline{\phi_m} \approx 0.97$, $St^+ = 30$
Lee & Lee (2015)	HC	$\overline{\phi_m} \approx 0.3$, $St^+ = 0.5$	$\overline{\phi_m} \approx 0.3$, $St^+ = 5$–125
Picano *et al.* (2015)	HC	$\overline{\phi_m} = 0.05$–0.1, $St^+ \approx 5.6$	$\overline{\phi_m} = 0.2$, $St^+ \approx 8.0$
Li *et al.* (2016)	DFBL	—	$\overline{\phi_m} = 0.1$–1, $St = 10$–30
Kasbaoui (2019)	HSF	$\overline{\phi_m} = 0.5$, $St_\eta = 0.06$	$\overline{\phi_m} \approx 0.13$, $St_\eta = 0.19$
Muramulla *et al.* (2020)	VC	—	$\overline{\phi_m} \leqslant 13.5$, $St^+ = 5$–420
Costa *et al.* (2021)	HC	$\overline{\phi_m} \approx 0.03$, $St^+ = 50$	$\overline{\phi_m} \approx 0.34$, $St^+ = 50$
Yu *et al.* (2021)	VC	$\chi_2 > 1.55$	$\chi_2 < 1.55$
Gao *et al.* (2023)	HOC	—	$\overline{\phi_m} = 0.024$, $St^+ = 6.0$ $\overline{\phi_m} = 0.14$, $St^+ = 448$

Table 1. Summary of previous work. Here, 'VC', 'HC', 'HSF', 'DFBL' and 'HOC' denote vertical channel, horizontal channel, homogeneous shear flow, developing flat-plate boundary layer and horizontal open channel, respectively; d_p is the particle diameter, l_e is the integral length scale, Re_p is the particle Reynolds number, η is the Kolmogorov length scale, $\overline{\phi_m}$ is the bulk mean particle mass loading, χ_2 is a dimensionless parameter proportional to Re_p, and St_η, St^+, St are the particle Stokes numbers defined by different characteristic flow time scales.

flows laden with sub-Kolmogorov-sized glass and copper particles at friction Reynolds number 600. They found that the addition of particles appears to attenuate turbulent intensity, with the degree of attenuation increasing with mass loadings ranging from 0.02 to 0.8. Similar results were also observed in other experiments (Kussin & Sommerfeld 2002; Li *et al.* 2012) and PP-DNS (Li *et al.* 2016; Muramulla *et al.* 2020). However, regarding dense dispersion, particle volume and mass loading exhibit non-monotonic behaviour in turbulence modulation. For example, PR-DNS studies of turbulent channels laden with finite-size (large) particles revealed that particles with small volume fractions tend to enhance turbulence, while the opposite trends were observed at large volume fractions (Picano *et al.* 2015; Costa *et al.* 2021; Yousefi *et al.* 2023). The studies mentioned above regarding turbulence modulation are summarized in table 1.

It is also noteworthy that in turbulent wall-bounded flows, turbulence modulation can result from the interaction between the particles and near-wall turbulent coherent structures. For example, PP-DNS studies of turbulent planar Couette flows by Richter & Sullivan (2013, 2014) have revealed that particles tend to attenuate near-wall swirling motions, particularly hairpin structures, leading to a decrease in the turbulent Reynolds stress. In a channel flow laden with super-Kolmogorov-sized particles, the disruption of the near-wall coherent structures is substantial, resulting in increased spacing between low- and high-speed streaks compared to single-phase flow (Costa *et al.* 2021). This

increase in spacing is also observed in channel flow laden with sub-Kolmogorov-sized particles, which can give rise to a greater reduction of Reynolds shear stress and partial relaminarization of the near-wall flow (Dave & Kasbaoui 2023).

Since inter-particle electrostatic forces are ubiquitous and modify the distribution and aggregation of particles remarkably, it is certainly expected that turbulence modulation by charged particles differs significantly from that by uncharged particles. Undoubtedly, the emergence of particle–electrostatics interactions poses new challenges and is more difficult to address than ordinary particle-laden turbulence. Using Reynolds-averaged Navier–Stokes (RANS) based simulations of particle electrification in wind-blown sand (also known as sand saltation), Zheng *et al.* (2003) and Zheng, Huang & Zhou (2006) demonstrated that the mean streamwise wind velocity is significantly reduced (increased) by positively (negatively) charged sand particles. However, turbulent fields cannot be obtained in their simulations due to the use of the RANS model. To the best of our knowledge, there is no systematic study on the turbulence modulation by charged inertial particles. Until now, the underlying mechanisms behind how charged particles modulate turbulence remain less understood. To address this issue, we aim to perform a series of large-domain PP-DNS of turbulent channel flows at a friction Reynolds number of approximately 540, laden with bidisperse uncharged and charged particles. This affords an opportunity to quantify the role of inter-particle electrostatic forces in both turbulent intensity and structure.

The rest of the paper is organized as follows. In § 2, we provide a detailed description of the large-domain PP-DNS. Next, the effects of inter-particle electrostatic forces on the mean flow and fluctuating velocities, interphase momentum and energy transfer, turbulent kinetic energy budget, as well as premultiplied spectra and autocorrelation functions, are presented and discussed in detail in §§ 3.1–3.3, respectively. Finally, main conclusions are summarized in § 4.

2. Methods

We use the numerical method developed by Zhang *et al.* (2023) to elucidate the influence of inter-particle electrostatic forces on turbulence modulation by inertial particles. This approach relies on the Eulerian–Lagrangian PP-DNS framework, which encompasses particle–turbulence and particle–electrostatics two-way coupling as well as inter-particle collisions. A comprehensive description of this method is provided in Zhang *et al.* (2023); however, we offer a brief summary here. The incompressible carrier fluid phase is described by the continuity and Navier–Stokes equations, representing mass and momentum conservation,

$$\boldsymbol{\nabla}\cdot\boldsymbol{u}=0,\quad \frac{\partial \boldsymbol{u}}{\partial t}+(\boldsymbol{u}\cdot\boldsymbol{\nabla})\boldsymbol{u}=-\frac{1}{\rho_f}\boldsymbol{\nabla}p+\nu\,\boldsymbol{\nabla}^2\boldsymbol{u}+\boldsymbol{f}, \tag{2.1}$$

where $\boldsymbol{u}=(u,v,w)$ is the fluid velocity, p is the pressure, ρ_f is the fluid mass density, and ν is the fluid kinematic viscosity. In (2.1), $\boldsymbol{f}=-\sum_k^{n_p}\boldsymbol{f}_D^k/(\rho_f V_{cell})$ represents the feedback force exerted by particles per unit mass of the fluid phase, where $\boldsymbol{f}_D^k$ is the hydrodynamic drag force acting on the kth particle within a computational cell of volume V_{cell} containing n_p particles. This feedback force is accounted for by a point-force approximation because the diameters d_p of the particles considered herein are smaller than or comparable to both the Kolmogorov scale of the fluid flow and the minimum grid spacing (Elghobashi 1994; Balachandar & Eaton 2010). The force density source term $\boldsymbol{f}$ is computed utilizing the particle-in-cell method, whereby the drag force is projected

onto the eight grid points surrounding each particle, as used in Squires & Eaton (1990), Gualtieri *et al.* (2013), Muramulla *et al.* (2020), Gao *et al.* (2023), and so on.

The turbulent channel flow is driven by a uniform pressure gradient, dynamically adjusting over time to maintain a constant bulk velocity (Lee & Moser 2015). Periodic boundary conditions are imposed in the streamwise and spanwise directions, while the top and bottom walls are subject to no-slip and no-penetration boundary conditions. The Eulerian flow is computed using a standard second-order finite-difference method on a staggered Cartesian mesh, together with a pressure-projection method based on fast Fourier transforms (Kim & Moin 1985; Schumann & Sweet 1988; Costa 2018).

Small rigid spherical particles, whether charged or uncharged, are tracked individually using the Lagrangian point-particle approximation. Given that the particle mass density ρ_p is much larger than the fluid mass density ρ_f, we consider only the drag force and inter-particle electrostatic force in the equation of particle motion according to Newton's second law (Maxey & Riley 1983; Armenio & Fiorotto 2001; Di Renzo & Urzay 2018; Boutsikakis *et al.* 2022),

$$\frac{\mathrm{d}\boldsymbol{x}_p}{\mathrm{d}t} = \boldsymbol{u}_p, \quad \frac{\mathrm{d}\boldsymbol{u}_p}{\mathrm{d}t} = \frac{1 + 0.15\, Re_p^{0.687}}{t_p}\left(\boldsymbol{u}_{f@p} - \boldsymbol{u}_p\right) + \frac{q\boldsymbol{E}}{m_p}, \tag{2.2}$$

where $\boldsymbol{x}_p$ is the particle position, $\boldsymbol{u}_p$ is the particle velocity, $Re_p = d_p\,|\boldsymbol{u}_{f@p} - \boldsymbol{u}_p|/\nu$ is the particle Reynolds number (Schiller & Naumann 1935; Lavrinenko, Fabregat & Pallares 2022), $t_p = d_p^2\rho_p/(18\nu\rho_f)$ is the particle inertial response time (e.g. Maxey 1987; Eaton & Fessler 1994), $\boldsymbol{u}_{f@p}$ is the fluid velocity at the particle position, q is the electrical charge of the particle, $\boldsymbol{E} = (e_{x@p}, e_{y@p}, e_{z@p})$ is the electric field at the particle position, and m_p is the particle mass.

It should be noted that an accurate evaluation of the drag force on particles requires that $\boldsymbol{u}_{f@p}$ is the undisturbed fluid velocity at the particle position. Consequently, a correction scheme for two-way coupled point-particle simulation is needed (e.g. Esmaily & Horwitz 2018; Muramulla *et al.* 2020). In this study, however, no correction method for calculating the undisturbed fluid velocity is employed. This reason is that when particles are smaller than the grid spacing, the error stemming from the usage of the distributed velocity is small (Horwitz & Mani 2016). In addition, the Saffman lift force is not considered herein because its magnitude is much smaller than the drag force when $d_p^+ < 1$ (Marchioli & Soldati 2002; Costa, Brandt & Picano 2020).

This motion equation is advanced in time utilizing a fourth-order Runge–Kutta scheme. The drag force is calculated using the Stokes drag law, incorporating the most commonly used Schiller–Naumann correlation to account for the nonlinear drag effects at finite particle Reynolds number (Schiller & Naumann 1935). The inter-particle electrostatic forces are computed by the particle-particle-particle mesh ($\mathrm{P^3M}$) method by assuming that the walls are conducting (i.e. zero electric potential), where both short- and long-range Coulomb interactions are explicitly accounted for (Kolehmainen *et al.* 2016; Sippola *et al.* 2018). In line with numerous previous studies (e.g. Wang & Richter 2019*b*; Jie *et al.* 2022; Motoori, Wong & Goto 2022; Gao *et al.* 2023), gravitational settling is excluded to emphasize the effects of inertia and electrostatic interactions. Additionally, both inter-particle and particle–wall collisions are considered to be perfectly elastic using the 'hard-sphere' approach (Grosshans & Papalexandris 2017). This is because there is a negligible difference in particle behaviour between elastic and inelastic collisions (Sardina *et al.* 2012; Johnson, Bassenne & Moin 2020). Inter-particle collisions are predominantly binary due to the dilute particle loading (Wang, Wexler & Zhou 2000), and they are detected using the Eulerian-mesh-based method (see Capecelatro & Desjardins 2013).

Case	Re_τ	u_τ	$\overline{\phi_m}$ ($\times 10^{-1}$)	$\overline{\phi_V}$ ($\times 10^{-4}$)	St^+	d_p^+	ρ_p/ρ_f	q (pC)	$\overline{St_{el}}$ ($\times 10^{-2}$)
C0	540	0.054	—	—	—	—	—	—	—
C1	530	0.053	0.22, 2.27	0.10, 1.03	25, 120	0.45, 0.99	2200	0, 0	0, 0
C2	553	0.055	0.22, 2.27	0.10, 1.03	25, 120	0.45, 0.99	2200	−0.02, +0.11	0.84, 5.94

Table 2. Summary of the simulated cases. Here, Re_τ is the friction Reynolds number, u_τ is the fluid friction velocity, $\bar{\phi}_m$ ($\bar{\phi}_V$) is the bulk mean particle mass loading (volume fraction), St^+ and d_p^+ are the particle's Stokes number and dimensionless diameter calculated by viscous scales, ρ_p/ρ_f is the particle-to-fluid density ratio, q is the amount of charge on the single particle, and $\overline{St_{el}}$ is the bulk mean electrostatic Stokes number.

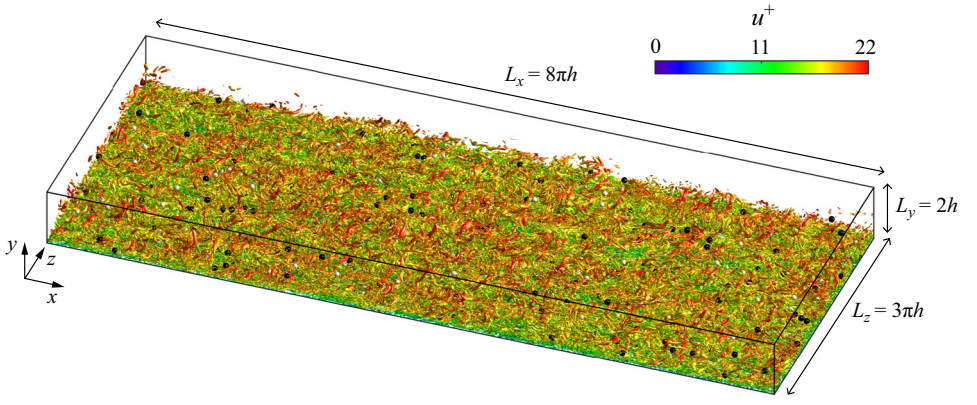

Figure 1. Visualization of case C1 at $t^+ \approx 1.5 \times 10^4$. The vortical structures within the lower half of the channel are visualized by the Q-criterion ($Q = 25$) and coloured with instantaneous streamwise velocity normalized by the friction velocity ($u^+ = u/u_\tau$). Black (white) spheres denote the larger (smaller) particles with wall distance below $h/2$ ($h = 0.2$ m), where only one out of every twenty thousand particles is shown for clarity.

Periodic boundary conditions are applied to particles in both the streamwise and spanwise directions, while the top and bottom walls are subject to reflective boundary conditions.

As presented in table 2, the unladen turbulent channel flow (case C0) is simulated at friction Reynolds number $Re_\tau \equiv u_\tau h/\nu \approx 540$, where $u_\tau = (\nu\, \mathrm{d}\langle u\rangle/\mathrm{d}y|_{y=0})^{1/2}$ (e.g. Vreman 2015), h and ν represent the fluid friction velocity, channel half-width and fluid kinematic viscosity, respectively. The simulation domain is set to $8\pi h$ in the streamwise (x) direction, $2h$ in the wall-normal (y) direction, and $3\pi h$ in the spanwise (z) direction (see figure 1), which is sufficiently large to capture the largest outer-layer flow structures (Lee & Moser 2015). A uniform grid is employed in the x- and z-directions, with grid spacings $\Delta x^+ = \Delta x/\delta_\nu = 9.00$ and $\Delta z^+ = \Delta z/\delta_\nu = 5.06$, while the grid is stretched in the y-direction with $\Delta y^+ = \Delta y/\delta_\nu$ ranging from 0.43 to 4.75 (viscous length scale $\delta_\nu = \nu/u_\tau$). As a result, the numbers of grid points in the x-, y- and z-directions are $N_x = 1536$, $N_y = 384$ and $N_z = 1024$, respectively.

In comparison to the unladen case C0, we examine two cases of particle-laden turbulent channel flows: one laden with uncharged bidisperse particles (case C1) and the other with charged bidisperse particles (case C2). Notably, the choice of a bidisperse particle system is motivated by two main reasons. First, in both industrial and natural systems, particles are always polydisperse, exhibiting distinct behaviours from monodisperse particles (e.g. Zhou, Wexler & Wang 2001). Second, in many situations, such as those encountered

in dust storms, the low volume fraction of particles (i.e. dilute regime) often results in only binary inter-particle collisions (Zhang & Zhou 2023; Zhang *et al.* 2023). Thus the mixing and dispersion of particles in the flow are typically analysed by considering the relative motion of particle pairs. Importantly, the polydisperse statistics can be derived from appropriate integrals of bidisperse statistics, weighted based on the size distribution of the particles (Dhariwal & Bragg 2018). Thus under such conditions, turbulent flows containing polydisperse particles can be effectively simplified into a bidisperse system.

In both laden cases, the particle-to-fluid density ratio for all particles is set to $\rho_p/\rho_f = 2200$, which is consistent with the density ratio of sand particles to air in natural wind-blown sand movements (Zheng 2009). The bidisperse particles consist of two distinct particle types characterized by viscous Stokes numbers $St^+ = t_p/t_\nu$ with values 25 and 120, corresponding to particle diameters 164 µm and 360 µm, respectively. Here, $t_p = d_p^2\rho_p/(18\nu\rho_f)$ and $t_\nu = \nu/u_\tau^2$ are the particle inertial response time and fluid viscous time scale, respectively. Specifically, the dimensionless particle diameters $d_p^+ = d_p/\delta_\nu$ for the larger and smaller particles are 0.45 and 0.99, respectively, both of which are smaller than the Kolmogorov scale of the fluid flow. The number of both larger and smaller particles is 1.60×10^7, with corresponding bulk mean particle mass loading (volume fraction) $\overline{\phi_m}$ ($\overline{\phi_V}$) having values 2.27×10^{-1} and 0.22×10^{-1} (1.03×10^{-4} and 0.10×10^{-4}). The particle mass loading at the wall-normal location y is defined as $\phi_m \equiv \rho_p/\rho_f\phi_V$ (e.g. Hwang & Eaton 2006; Yousefi *et al.* 2023), where $\phi_V = \sum_{i=1}^{2} N_{p,i}V_{p,i}/(L_xL_z\,\mathrm{d}\xi)$ is the particle volume fraction within the wall-normal location $[y - \mathrm{d}\xi/2, y + \mathrm{d}\xi/2]$, with $\mathrm{d}\xi$ being the radius of the smaller particle. Here, $N_{p,i}$ represents the total number of the ith particle class within this wall-normal position range, and $V_{p,i}$ denotes the volume of a particle of the ith particle class.

In case C2, charge transfer during inter-particle and particle–wall collisions is not considered, as in many previous studies (e.g. Di Renzo & Urzay 2018; Grosshans *et al.* 2021; Boutsikakis *et al.* 2022). Consequently, all particles carry constant surface charge density $\sigma_s = 0.27\,\mu\mathrm{C\,m^{-2}}$, which is 0.01 times the maximum surface charge density for spherical particles in a normal atmosphere (Hamamoto, Nakajima & Sato 1992). It is well known that particle electrification exhibits a 'size-dependent effect', where larger particles tend to charge positively while smaller particles tend to charge negatively (Lacks & Sankaran 2011). Therefore, each larger (smaller) particle carries a charge +0.11 pC (−0.02 pC). The relative importance of particle electrical effects and particle inertia can be quantified by the electrostatic Stokes number St_{el}, which is defined by the ratio of the particle inertial response time τ_p to the characteristic time scale of inter-particle electrostatic interactions t_{el}, i.e. $St_{el} = t_p/t_{el}$. Using standard dimensional analysis, we have $t_{el} = (6\pi\varepsilon_0 m_p/(nq^2))^{1/2}$, where n and ε_0 are the particle number density and the permittivity of the vacuum, respectively. In case C2, the bulk mean St_{el} is 0.84×10^{-2} for the smaller particles and 5.94×10^{-2} for the larger particles, indicating a noticeable inter-particle electrostatic interaction (e.g. Grosshans *et al.* 2021; Boutsikakis *et al.* 2022; Zhang *et al.* 2023).

In cases C1 and C2, once the unladen case C0 reaches a fully developed state (denoted by $t^+ = t/t_\nu = 0$), particles are released randomly into the entire computational domain, with their initial velocities matching the fluid velocity at the particles' positions. Subsequently, the particle-laden turbulent channel flow continues to evolve until it achieves a statistically stationary state at approximately $t^+ = 1.5 \times 10^4$ (or equivalently, global eddy-turnover time $h/u_\tau \approx 28$). In this study, the numerical algorithm is implemented in

Fortran 90 computer code and parallelized using the message passing interface based on a two-dimensional pencil-like domain decomposition (Costa 2018). The typical duration of a simulation is approximately 64 000 CPU hours on 512 cores (Intel Xeon Platinum 9242 CPU @ 2.30 GHz). In practice, ensemble averages for any statistics, denoted by angle brackets $\langle \cdot \rangle$, are performed numerically by spatial averaging within the horizontal plane, and temporal averaging over 11 equally spaced snapshots within the time interval $t^+ \in [1.0 \times 10^4, 1.5 \times 10^4]$, spanning more than nine global eddy-turnover times.

3. Results

3.1. *Mean flow and fluctuating velocities*

To assess whether inter-particle electrostatic forces significantly affect turbulence modulation by particles, we begin by presenting the instantaneous distribution of near-wall streamwise velocity fluctuations in the horizontal x–z plane, as shown in figure 2. It is evident that charged and uncharged particles exhibit distinct modulation of the near-wall flow field. In all cases C0–C2, highly streamwise-elongated, alternating low- and high-speed streaks are present near the wall (e.g. Zhao *et al.* 2010; Zheng, Feng & Wang 2021). However, compared to the unladen case C0, when the flow is laden with uncharged particles, such streamwise-elongated flow streaks become longer and wider (Zhao *et al.* 2010). By contrast, when the particles are charged, the shapes of the fluid streaks are further expanded (a quantitative comparison using two-point autocorrelation functions is given in § 3.3), indicating that inter-particle electrostatic forces indeed have a dramatic influence on turbulence modulation.

Figure 3(*a*) illustrates wall-normal profiles of the inner-scaled mean streamwise fluid velocities for various cases. Compared to case C0, the inner-scaled mean streamwise fluid velocity for case C1 exhibits a noticeable increase in the outer layer, and agrees well with numerous simulated and experimental results involving uncharged inertial particles with diameter smaller than the Kolmogorov length scales of turbulence (e.g. Pan & Banerjee 1996; Kaftori, Hetsroni & Banerjee 1998; Dritselis & Vlachos 2008; Zhao *et al.* 2013; Li *et al.* 2016; Gao *et al.* 2023). This increase in the inner-scaled mean velocity can be attributed to a reduction in the fluid friction velocity since the mass flow rate is kept constant for all cases. In contrast, the overall inner-scaled mean velocity for case C2 is considerably shifted towards lower values, suggesting an increase in the fluid friction velocity. For comparison, figure 3(*b*) displays the outer-scaled mean streamwise fluid velocities. It is shown that the outer-scaled mean velocities exhibit significant (slight, see inset) differences in the near-wall (outer) region.

It is known that the effect of particles on the mean streamwise velocity is determined by two physical mechanisms: (1) particles directly affect the local fluid velocity through interactions with turbulence; and (2) the presence of particles alters the local viscous transport, thus modifying the velocity gradient of the flow field (e.g. Kaftori *et al.* 1998; Peng, Ayala & Wang 2019). In such a case, particle mass loading plays a dominant role in the mean streamwise velocity. The PP-DNS studies of particle-laden turbulent channel flow conducted by Li *et al.* (2001) reveal that for smaller particle mass loadings ($\phi_m \sim 0.2$–0.4), particles increase the mean streamwise velocity, while the opposite effect is observed for the larger particle mass loading ($\phi_m \sim 2$).

Figure 4 shows comparisons of the wall-normal profiles of particle mass loading between cases C1 and C2. In case C1, particles tend to migrate towards the wall, resulting in the mean particle concentration (i.e. mass loading) being maximized within the viscous layer, a phenomenon known as turbophoresis (Caporaloni *et al.* 1975; Reeks 1983).

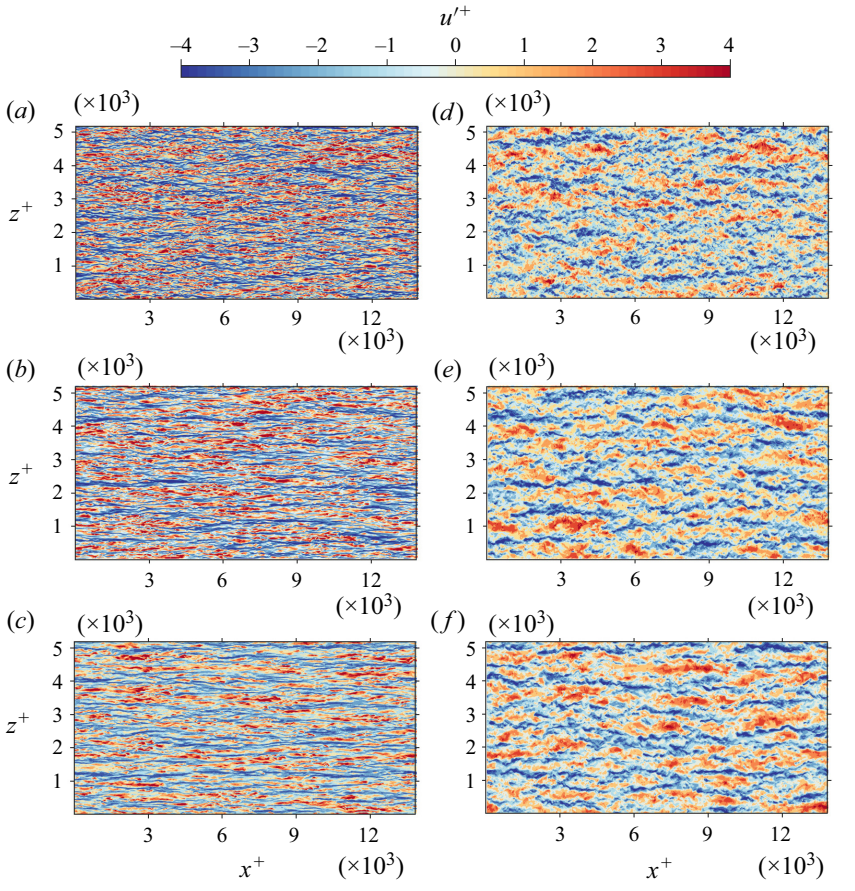

Figure 2. Instantaneous snapshots of the fluctuating streamwise fluid velocity u'^+ in the streamwise–spanwise (x–z) planes at $t^+ \approx 1.5 \times 10^4$ (not to scale). (a–c) Snapshots of the fluctuating streamwise fluid velocity at $y^+ = 10.5$ for the cases C0, C1 and C2, respectively. (d–f) Same as (a–c) but for the fluctuating streamwise fluid velocity at $y^+ = 103.1$.

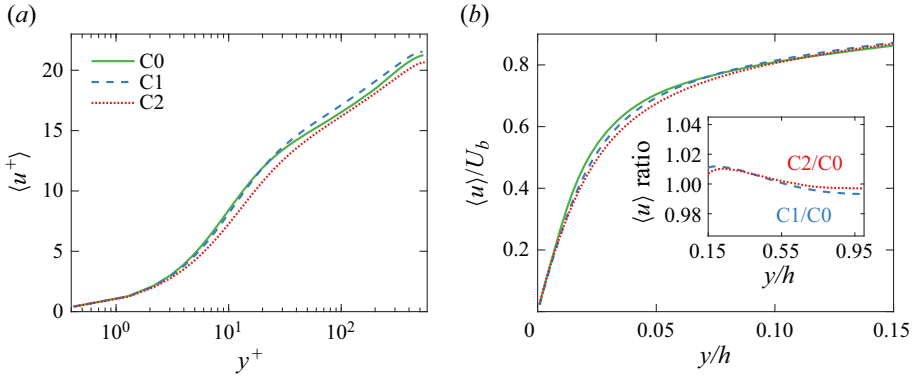

Figure 3. Wall-normal profiles of the (a) inner-scaled and (b) outer-scaled mean streamwise fluid velocities for cases C0–C2. The inset shows the ratio of the mean streamwise fluid velocity between cases C1 and C0 (dashed line) and between C2 and C0 (dotted line).

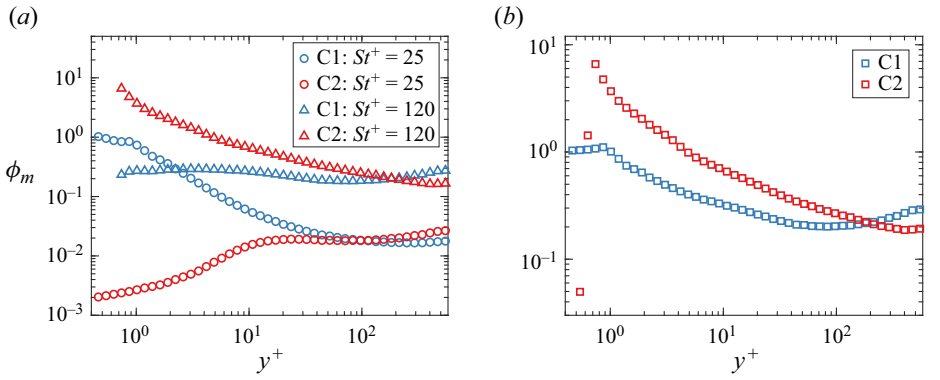

Figure 4. (*a*) Wall-normal profiles of particle mass loadings for the smaller and larger particles in cases C1 and C2. (*b*) Wall-normal profiles of the total particle mass loadings for cases C1 and C2.

Additionally, smaller particles exhibit stronger turbophoresis than larger ones. This can be attributed to two reasons: (1) turbophoresis is most pronounced when the particle response time scale matches the characteristic time scale of the buffer layer, corresponding to a particle Stokes number $St^+ \sim 10$–50 (Sardina *et al.* 2012); and (2) larger particles experience inter-particle collisions due to larger volume fractions, which tend to bring the concentration profile towards a uniform profile (Johnson *et al.* 2020). In comparison to case C1, positively charged larger particles in case C2 exhibit an increase (decrease) in mass loading in the region $y^+ \lesssim 180$ ($y^+ \gtrsim 180$), while negatively charged smaller particles in case C2 show a decrease (increase) in mass loading in the region $y^+ \lesssim 100$ ($y^+ \gtrsim 100$). This leads to an overall increase in particle mass loading ϕ_m from $\lesssim 1$ to nearly 8 in the region of $y^+ \lesssim 200$ (figure 4*b*). Such changes in particle mass loadings due to inter-particle electrostatic forces can be explained by the direction of the wall-normal electric field at the particles' positions, $e_{y@p}$. As depicted in figure 5, the probability density functions (p.d.f.s) of $e_{y@p}$ for both smaller and larger particles are distributed at negative $e_{y@p}$ in the bulk of the channel, with a zero-mean $e_{y@p}$ only at the channel centreline. In such instances, negatively charged smaller (positively charged larger) particles experience electrostatic forces pointing towards the channel centreline (wall), resulting in an electrostatic drift towards the channel centreline (wall).

Therefore, we can conclude that the opposite trends in modulation of mean streamwise velocity between uncharged and charged particles is attributed to substantial changes in particle mass loading induced by inter-particle electrostatic forces.

In addition to modulating the mean streamwise velocity, charged particles have a remarkable influence on turbulent fluctuations, as depicted in figure 6. In contrast to case C0, the root mean square (r.m.s.) streamwise fluctuating velocity is reduced in the near-wall region ($y^+ \lesssim 20$) in the presence of uncharged particles, with a slight enhancement in the outer region ($y^+ \gtrsim 20$). Conversely, the r.m.s. wall-normal and spanwise fluctuating velocities, as well as Reynolds stress, are largely diminished throughout the entire channel. These results are consistent with previous studies on turbulent channel flows laden with uncharged particles (e.g. Li *et al.* 2001; Dritselis & Vlachos 2008). Importantly, when compared to case C1, all r.m.s. fluctuating velocities and Reynolds stress in the region $y^+ \lesssim 200$ are significantly suppressed for case C2, with negligible effects in the region $y^+ \gtrsim 200$. This implies that inter-particle electrostatic forces appear to further inhibit turbulent fluctuations.

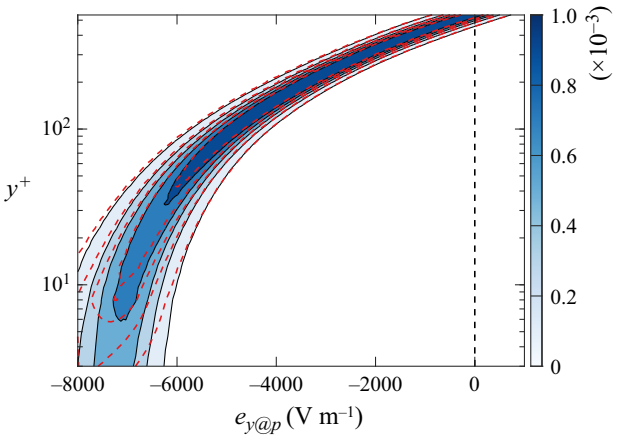

Figure 5. The p.d.f.s of the wall-normal electric field at the positions of the particles $e_{y@p}$ for case C2. Here, the black solid lines and red dashed lines represent the p.d.f. contours for the smaller and larger particles, respectively.

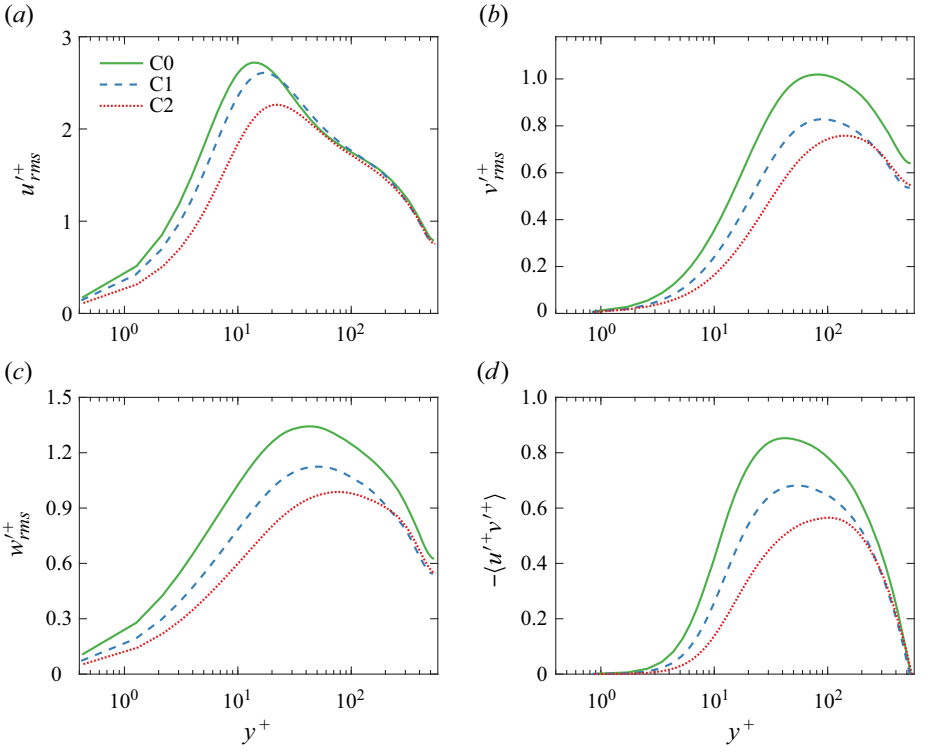

Figure 6. Wall-normal profiles of the r.m.s. (*a*) streamwise, (*b*) wall-normal and (*c*) spanwise fluctuating velocities, as well as (*d*) Reynolds stress $-\langle u'^{+}v'^{+}\rangle$ for cases C0–C2.

The attenuation of turbulence by charged particles can be explained by variations in the parameters that control turbulence modulation. For the flow and particle conditions examined herein, the main control parameters are particle Reynolds number and mass loading (Peng *et al.* 2019). It is widely acknowledged that: (1) particles with low Reynolds

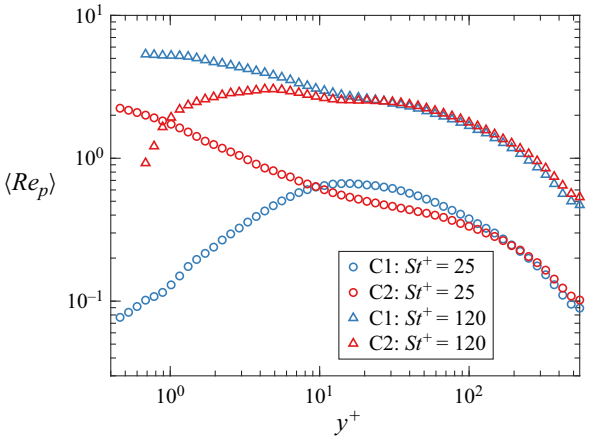

Figure 7. Wall-normal profiles of the average particle Reynolds number $\langle Re_p \rangle$ for the smaller and larger particles in cases C1 and C2.

numbers suppress turbulence, whereas those with higher Reynolds numbers, typically larger than 300 for isolated particles (Hetsroni 1989; Johnson & Patel 1999) but small for particle clusters (Capecelatro *et al.* 2014, 2015), enhance turbulence through wake shedding (Hetsroni 1989; Yu *et al.* 2021); (2) as particle mass loading increases, turbulence modulation by particles becomes increasingly pronounced (Kulick *et al.* 1994; Li *et al.* 2001; Zhao *et al.* 2013; Costa *et al.* 2021). In this study, as shown in figure 7, although the particle Reynolds numbers near the wall are altered considerably when the particles are charged, their values remain below 5, indicating the absence of wake shedding. Therefore, according to the aforementioned criteria, whether particles are charged or not, they are believed to suppress turbulence fluctuations. On the other hand, the particle mass loading is significantly increased near the wall but is slightly changed in the outer region (figure 4*b*) when particles are charged. This results in charged particles having a substantial suppression (negligible influence) on turbulence near the wall (in the outer region) compared to the uncharged particles.

For completeness, the basic statistics of the particulate phase are also shown in figure 8. As expected, when particles are uncharged, the smaller particles follow the fluid phase fairly well, but the larger particles travel faster than the fluid phase below $y^+ \approx 15$, in line with previous studies (e.g. Li *et al.* 2012; Fong, Amili & Coletti 2019). When particles are charged, the mean particle streamwise velocity of the smaller particles increases, while that of the larger particles decreases below $y^+ \approx 15$; both exceed the mean fluid streamwise velocity within this layer (figure 8*a*). As a result, the magnitude of the mean particle-to-fluid relative velocity, $\langle \Delta u^+ \rangle = \langle u^+_{f@p} \rangle - \langle u^+_p \rangle$, is increased (decreased) for the smaller (larger) particles (figure 8*b*). Under the influence of inter-particle electrostatic forces, the r.m.s. streamwise particle fluctuating velocity of the smaller particles is increased (decreased) below (above) $y^+ \approx 8$, while that of larger particles is decreased (remains unchanged) below (above) $y^+ \approx 30$ (figure 8*c*). Interestingly, the r.m.s. streamwise fluctuating velocity of the particulate phase is also larger than that of the fluid phase throughout the channel. Similar conclusions are found for the r.m.s. particle fluctuating velocity of the spanwise and wall-normal components (not shown for brevity), and particle Reynolds stress (figure 8*d*).

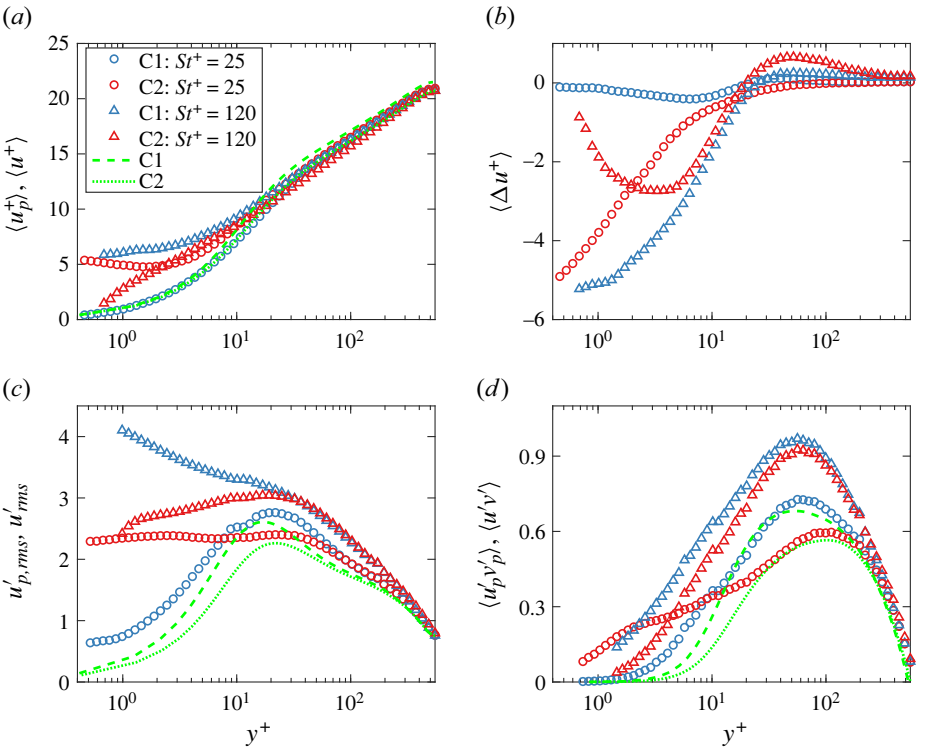

Figure 8. Wall-normal profiles of (*a*) the mean streamwise particle velocity $\langle u_p^+ \rangle$, (*b*) the mean particle-to-fluid relative velocity $\langle \Delta u^+ \rangle = \langle u_{f@p}^+ \rangle - \langle u_p^+ \rangle$, (*c*) the r.m.s. streamwise particle fluctuating velocity $u'_{p,rms}$ and (*d*) the particle Reynolds stress $-\langle u'_p v'_p \rangle$, for cases C1 and C2. Here, the dashed and dotted lines represent the corresponding statistics of the fluid phase.

3.2. *Interphase momentum and energy transfer*

To gain further insight, we next examine the streamwise momentum balance of the fluid phase (Picano *et al.* 2015; Peng *et al.* 2019; Costa *et al.* 2021; Gao *et al.* 2023),

$$\tau_T(y) = \underbrace{\rho_f \nu \frac{\partial \langle u \rangle}{\partial y}}_{\tau_\nu} \underbrace{- \rho_f \langle u'v' \rangle}_{\tau_R} + \underbrace{\rho_f \int_h^y \langle f_x \rangle \, \mathrm{d}y}_{\tau_p} = \tau_w \left(1 - \frac{y}{h}\right), \tag{3.1}$$

where $\langle f_x \rangle$ is the mean hydrodynamic force in the streamwise direction exerted on the fluid phase due to particles, and τ_T, τ_ν, τ_R and τ_p denote the total, fluid viscous, turbulent Reynolds and particle stresses, respectively. A detailed derivation of (3.1) is provided in Appendix A.

Figure 9(*a*) displays the streamwise momentum balance for various cases. It is evident that the total stress τ_T behaves as a straight line with slope $-1/h$ for different cases (see inset of figure 9*a*), suggesting that all simulations have attained the final steady state. The fluid viscous stress τ_ν dominates in the viscous sublayer but rapidly decreases to very small values as y increases, nearly unaffected by the presence of uncharged and charged particles. For case C0, the turbulent Reynolds stress τ_R increases with increasing y, peaks at $y/h \approx 0.8$, and then decreases, dominating in the outer region. In the presence of particles, the turbulent Reynolds stress follows a similar trend to that of unladen flow but is substantially reduced due to momentum extraction by particles, especially

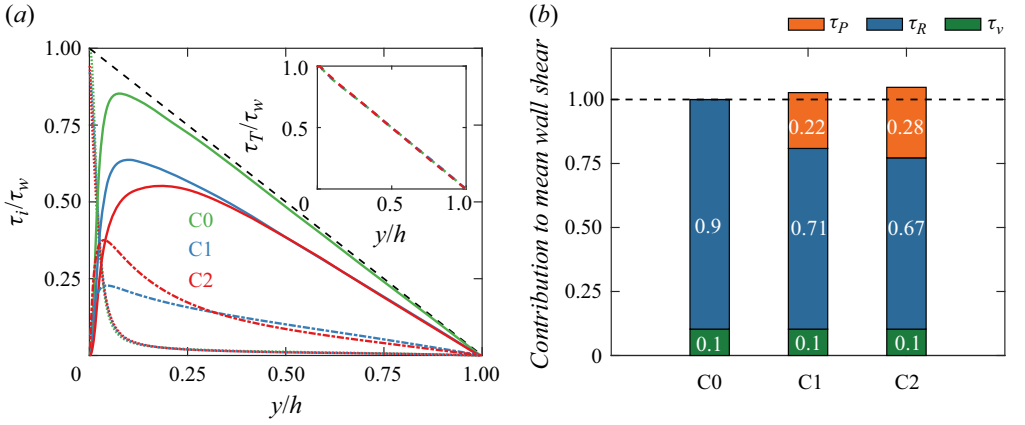

Figure 9. (*a*) Wall-normal profiles of the fluid viscous (dotted lines), turbulent Reynolds (solid lines) and particle stresses (dot-dashed lines), where the black dashed line denotes $\tau_w(1-y/h)$. The inset shows the summations of the fluid viscous, turbulent Reynolds and particle stresses for various cases. Here, green, blue and red lines denote cases C0, C1 and C2, respectively. (*b*) Relative contributions of different stresses in the stress budget to the mean wall friction, which is normalized by that of the unladen case, namely, $1/h\int_0^h 3(1-y/h)\tau_i\,\mathrm{d}y/(\rho_f u_{\tau,0}^2)$. Here, the contribution of the stress τ_i, $i\in\{P,R,\nu\}$, is evaluated by the weighted integral $1/h\int_0^h 3(1-y/h)\tau_i\,\mathrm{d}y$ (see Appendix B for details), and $u_{\tau,0}$ is the friction velocity for the unladen case C0.

when the particles are charged. The profiles of the particle stress τ_p resemble those of turbulent Reynolds stress but reach their maxima at a relatively low wall-normal location. In particular, when particles are charged, the particle stress is significantly enhanced below (and reduced above) $y/h\approx 0.3$, suggesting that inter-particle electrostatic forces facilitate the particles to extract momentum from the fluid phase near the wall.

The contribution of each stress to the overall drag is depicted in figure 9(*b*). For case C0, the contributions of viscous and turbulent Reynolds stresses are approximately 0.1 and 0.9, respectively. For case C1, the contribution of the viscous stress remains unchanged, but that of the turbulent Reynolds stress is reduced to approximately 0.71, resulting in the combined contribution of these two stresses (i.e. the fluid stress) being smaller than the overall drag in case C0. However, the contribution of the particle stress accounts for approximately 0.22, which counteracts the drag reduction resulting from fluid stress and leads to an overall increase in drag. For case C2, the reduction in the contribution of turbulent Reynolds stress is more prominent compared to case C1. However, due to a considerable increase in the particle stress, the overall drag is further increased. This demonstrates that inter-particle electrostatic forces increase the overall drag by indirectly enhancing the contribution of the particle stress.

Note that, compared to case C0, u_τ increases in case C2 (figure 3*a*), while the contribution of fluid stress to overall drag decreases (figure 9*b*). However, these two situations are not contradictory. Specifically, u_τ represents only the variation of τ_ν at the wall position, and although it increases for case C2, the overall change in the wall-normal profile of τ_ν is almost negligible. Therefore, the contribution of τ_ν to overall drag remains constant across all cases. In contrast, for case C2, the wall-normal profile of τ_R exhibits a significant downward shift, leading to a decrease in the relative contribution of overall drag by Reynolds stress (and thus fluid stress).

It is worth remarking that although the presence of uncharged particles (case C1) enhances the total drag, it does not considerably modify the mean streamwise fluid velocity within the viscous sublayer and buffer region (figure 3*a*). This contrasts with

many other drag modulation mechanisms. For example, when channel flow is subjected to oscillatory spanwise wall motion, the drag decreases, and the thickness of the viscous sublayer is significantly reduced (Touber & Leschziner 2012). In turbulent channel flows with a riblet surface, a maximum drag reduction is reached when the so-called 'viscous regime' breaks down (Garcia-Mayoral & Jiménez 2011). Similarly, in turbulent pipe flows with three-dimensional sinusoidal roughness, the increase in wall drag is manifested as a downward shift in the wall-normal profile of the mean streamwise fluid velocity (Chan *et al.* 2015).

Apart from momentum exchange, kinetic energy exchange between the particulate phase and the fluid phase also arises due to the presence of relative velocity between them. The amounts of kinetic energy transferred from the local fluid to a particle and from a particle to the local fluid per unit time, denoted by powers W_p and W_f, are given by (Zhao *et al.* 2013; Li *et al.* 2016)

$$W_p = \frac{m_p(1 + 0.15\,Re_p^{0.687})}{t_p}\left(\boldsymbol{u}_{f@p} - \boldsymbol{u}_p\right)\cdot\boldsymbol{u}_p, \tag{3.2}$$

$$W_f = -\frac{m_p(1 + 0.15\,Re_p^{0.687})}{t_p}\left(\boldsymbol{u}_{f@p} - \boldsymbol{u}_p\right)\cdot\boldsymbol{u}_{f@p}. \tag{3.3}$$

Therefore, the net particle dissipation ε_p is expressed as the sum of W_p and W_f:

$$\varepsilon_p = W_p + W_f = \frac{m_p(1 + 0.15\,Re_p^{0.687})}{t_p}\left(\boldsymbol{u}_{f@p} - \boldsymbol{u}_p\right)\cdot(\boldsymbol{u}_p - \boldsymbol{u}_{f@p}). \tag{3.4}$$

Figure 10 illustrates the wall-normal profiles of powers $\langle W_p^+\rangle$ and $\langle W_f^+\rangle$, as well as particle dissipation $\langle\varepsilon_p^+\rangle$. As shown in figures 10(*a–c*), in the case of C1, values of $\langle W_p^+\rangle$, $\langle W_f^+\rangle$ and $\langle\varepsilon_p^+\rangle$ for larger particles (i.e. $St^+ = 120$) are much larger than those for small particles (i.e. $St^+ = 25$), especially in the near-wall region, in agreement with the results of Gao *et al.* (2023). This discrepancy arises because larger particles exhibit a greater particle-to-fluid relative velocity in the near-wall region (Kulick *et al.* 1994; Vance, Squires & Simonin 2006; Fong *et al.* 2019). Interestingly, in the case of C2, values of $\langle W_p^+\rangle$, $\langle W_f^+\rangle$ and $\langle\varepsilon_p^+\rangle$ for smaller particles are significantly enhanced, while those for larger particles are notably suppressed. This occurs because inter-particle electrostatic forces tend to enhance (inhibit) the particle-to-fluid relative velocity of smaller (larger) particles in the near-wall region (see figure 8*b*). However, compared to case C1, the total $\langle W_p^+\rangle$ and $\langle W_f^+\rangle$ are considerably enhanced when particles are charged (figures 10*d*,*e*). It should be emphasized that in the presence of particles, the total particle dissipation $\langle\varepsilon_p^+\rangle$ is non-zero, indicating that particles induce additional energy dissipation. Furthermore, when particles are charged, the extra dissipation caused by the particles is remarkably strengthened below $y^+ \approx 110$ (see figure 10*f*).

Similar to the transfer of kinetic energy, the fluctuating feedback force exists in the governing equation of the turbulent kinetic energy budget, and generally exhibits a dissipative effect. The balance equation of the turbulent kinetic energy $K = \langle\boldsymbol{u}'\cdot\boldsymbol{u}'\rangle/2$ for the channel flow is given by

$$P_K - D_K - \epsilon_K + \Psi_K = 0, \tag{3.5}$$

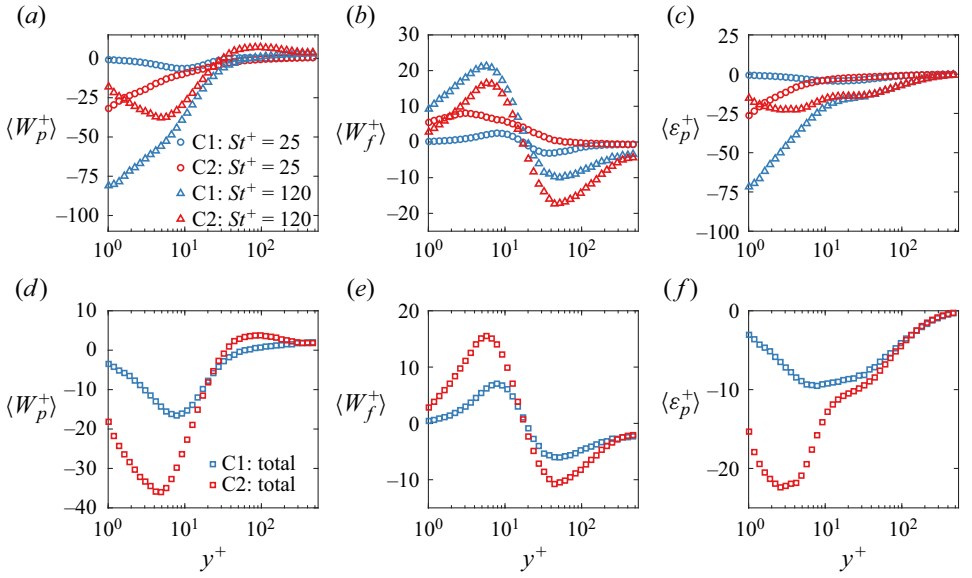

Figure 10. (*a–c*) Wall-normal profiles of the normalized powers $\langle W_p^+ \rangle$ and $\langle W_f^+ \rangle$, as well as particle dissipation $\langle \varepsilon_p^+ \rangle$ for the smaller and larger particles, in cases C1 and C2. (*d–f*) Same as (*a–c*), but for the total power and particle dissipation. Here, all powers and particle dissipations are normalized by $m_p u_\tau^2 / t_p$.

where

$$P_K = -\langle u'v' \rangle \frac{\partial \langle u \rangle}{\partial y}, \tag{3.6}$$

$$D_K = \frac{\partial}{\partial y} \left(\frac{1}{2} \langle (\boldsymbol{u}' \cdot \boldsymbol{u}') v' \rangle + \frac{\langle p'v' \rangle}{\rho_f} - \nu \frac{\partial \langle K \rangle}{\partial y} \right), \tag{3.7}$$

$$\epsilon_K = \nu \langle \nabla \boldsymbol{u}' : \nabla \boldsymbol{u}' \rangle, \tag{3.8}$$

$$\Psi_K = \langle \boldsymbol{u}' \cdot \boldsymbol{f}' \rangle. \tag{3.9}$$

Here, P_K, D_K, ϵ_K and Ψ_K represent the turbulent production, total turbulent diffusion, turbulent viscous dissipation and particle-induced energy sink term, respectively. The production term P_K represents the generation of velocity fluctuations through mean shear, which is a source term in (3.5). The diffusion term D_K redistributes energy with no net contribution. The energy injected via P_K is dissipated by turbulent dissipation ϵ_K and particle-induced energy sink Ψ_K.

The turbulent kinetic energy budget is depicted in figure 11. It is apparent that all terms in (3.5) are considerably influenced by the presence of particles. The addition of uncharged particles results in a reduction in the magnitudes of turbulent production, diffusion and dissipation. When particles are charged, these reductions become more prominent. The substantial reduction in turbulent production necessitates a reduction in viscous dissipation. In particular, the particle-induced energy sink plays a crucial role in turbulence attenuation. In a thin layer adjacent to the wall, where turbulent fluctuations are weak, fluid velocity fluctuations are produced mainly by particles. Therefore, velocity fluctuations of the fluid and particles are expected to be positively correlated within this thin layer, resulting in a positive Ψ_K (see Vreman 2015). However, Ψ_K is negative in the bulk of the channel flow, acting as a sink for turbulent kinetic energy (figure 11*d*).

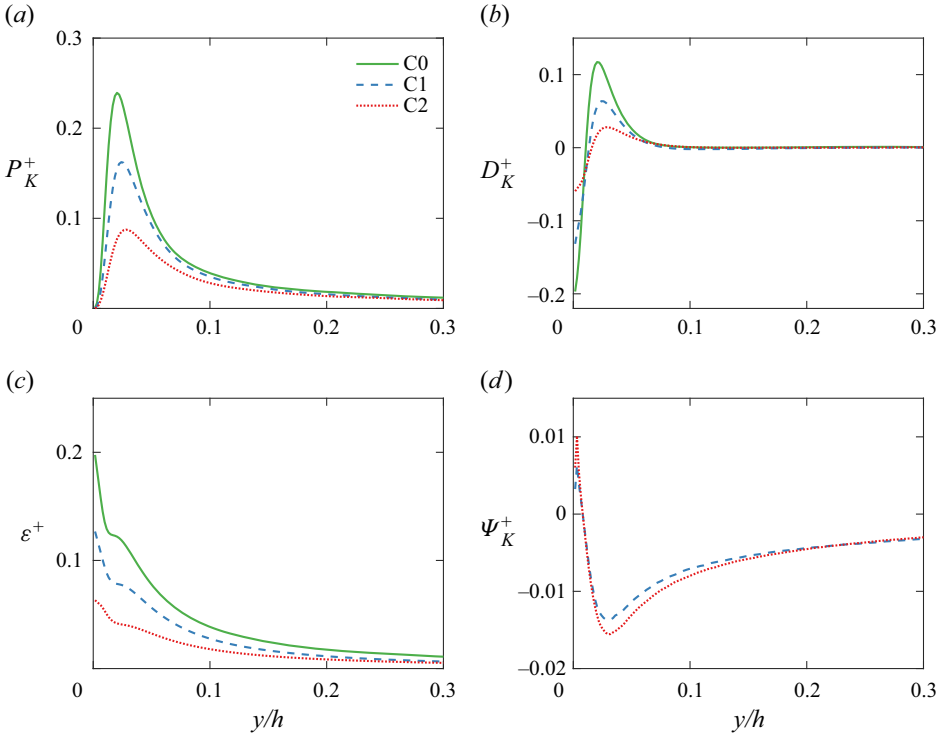

Figure 11. Turbulence kinetic energy budget in the near-wall region: (*a*) turbulence production P_K^+, (*b*) total diffusion D_K^+, (*c*) turbulence dissipation ε^+, and (*d*) particle-induced energy source term Ψ_K^+. Here, all terms are normalized by u_τ^4/ν.

In short, inter-particle electrostatic forces suppress turbulent production and enhance the particle-induced energy sink, thereby attenuating turbulence.

3.3. *Premultiplied spectra and autocorrelation functions*

To elucidate the role of inter-particle electrostatic forces in the modulating turbulence structure, we end by quantifying the premultiplied spectra and two-point autocorrelation functions of the fluctuating streamwise fluid velocity in this subsection. Figure 12 shows the premultiplied one-dimensional u-spectra $k_x\Phi_{uu}/u_\tau^2$ and $k_z\Phi_{uu}/u_\tau^2$, where $\Phi_{uu} = \langle \hat{u}'(k_z)\,\hat{u}'^*(k_z)\rangle$, with $\widehat{(\,)}$ and $(\,)^*$ representing the Fourier modes and complex conjugate, respectively (Pope 2000). For case C0 (figures 12*a*,*d*), the premultiplied spectra $k_x\Phi_{uu}/u_\tau^2$ and $k_z\Phi_{uu}/u_\tau^2$ exhibit a noticeable inner peak at wall-normal location $y^+ \approx 13$ and wavelengths $\lambda_x^+ \approx 1000$ and $\lambda_z^+ \approx 100$, consistent with existing results (Del Alamo & Jiménez 2003; Wang & Richter 2019*b*). The emergence of this inner peak is created by the self-sustaining near-wall cycle (e.g. Jiménez & Pinelli 1999; Schoppa & Hussain 2002; Hutchins & Marusic 2007). In addition, this inner peak corresponds to a spatial length of approximately $1.85h$ in the streamwise direction, and is commonly referred to as large-scale motions (LSMs; see Guala, Hommema & Adrian 2006). Notably, we do not observe distinct outer peaks in the premultiplied spectra, which correspond to the streamwise length scales exceeding $O(3h)$, and are generally termed very-large-scale motions or superstructures (Guala *et al.* 2006; Hutchins & Marusic 2007; Wang & Zheng

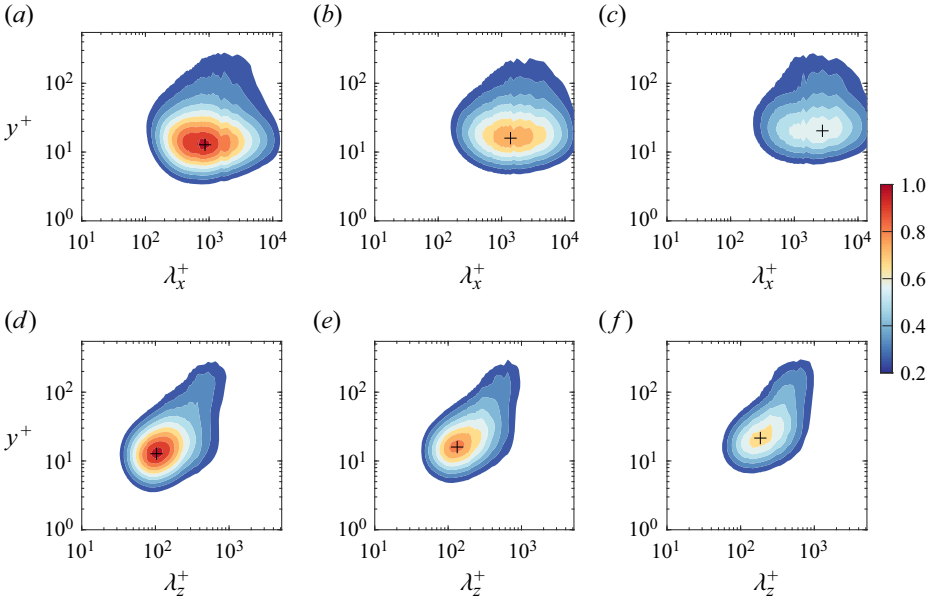

Figure 12. Premultiplied u-spectra as a function of wavelength and wall-normal location y^+: (*a*) $k_x\Phi_{uu}/u_\tau^2$ for case C0, (*b*) $k_x\Phi_{uu}/u_\tau^2$ for case C1, (*c*) $k_x\Phi_{uu}/u_\tau^2$ for case C2, (*d*) $k_z\Phi_{uu}/u_\tau^2$ for case C0, (*e*) $k_z\Phi_{uu}/u_\tau^2$ for case C1, and (*f*) $k_z\Phi_{uu}/u_\tau^2$ for case C2. Here, λ_x^+ and λ_z^+ denote streamwise and spanwise wavelengths, respectively. The values are normalized by the maximum value of the unladen flow. The plus signs (i.e. +) mark the peaks of the spectra.

2016). This happens because the energy content in the outer region continuously increases with increasing Reynolds number Re_τ, therefore outer peaks are typically more prominent at $Re_\tau \geqslant 1800$ (Duan *et al.* 2020; Yao, Chen & Hussain 2022). For case C1, although the wall-normal location of the inner peak remains almost unchanged, the peaks are shifted towards larger streamwise and spanwise wavelengths (i.e. $\lambda_x^+ \approx 1382$ and $\lambda_z^+ \approx 133$), and their magnitudes are significantly reduced (figures 12*b*,*e*).

It is demonstrated that inertial particles disrupt the self-sustaining near-wall cycle, where the dominant structures are the streamwise velocity streaks and quasi-streamwise vortices. Therefore, the changes in the premultiplied u-spectra $k_x\Phi_{uu}/u_\tau^2$ and $k_z\Phi_{uu}/u_\tau^2$ by uncharged particles can be physically explained as follows: uncharged high-inertia particles of $St^+ \gtrsim O(30\text{–}50)$ (i.e. smaller and larger particles in this study; see table 2) tend to reduce the strength and number of the quasi-streamwise vortices, as well as streamwise vorticity stretching and lift-up effects (Wang & Richter 2019*a*); as a result, the streamwise velocity streaks are thickened, but their fluctuating amplitudes are suppressed (Zhao *et al.* 2010), which is reflected by a weaker premultiplied spectrum peaked at a larger wavelength.

Additionally, since the particle mass loading close to the wall is increased by the inter-particle electrostatic forces (figure 4*b*), the thickening of the streamwise velocity streaks and the suppression of the strength of the quasi-streamwise vortices are even more pronounced for case C2. Therefore, the weakest spectral peaks among cases C0–C2 are located at $\lambda_x^+ \approx 2764$ and $\lambda_z^+ \approx 185$ (figures 12*c*,*f*). In short, inter-particle electrostatic forces seem to increase the length scale of LSMs in both the streamwise and spanwise directions, but reduce the intensity of LSMs in terms of indirect modulations of the self-sustaining near-wall cycle.

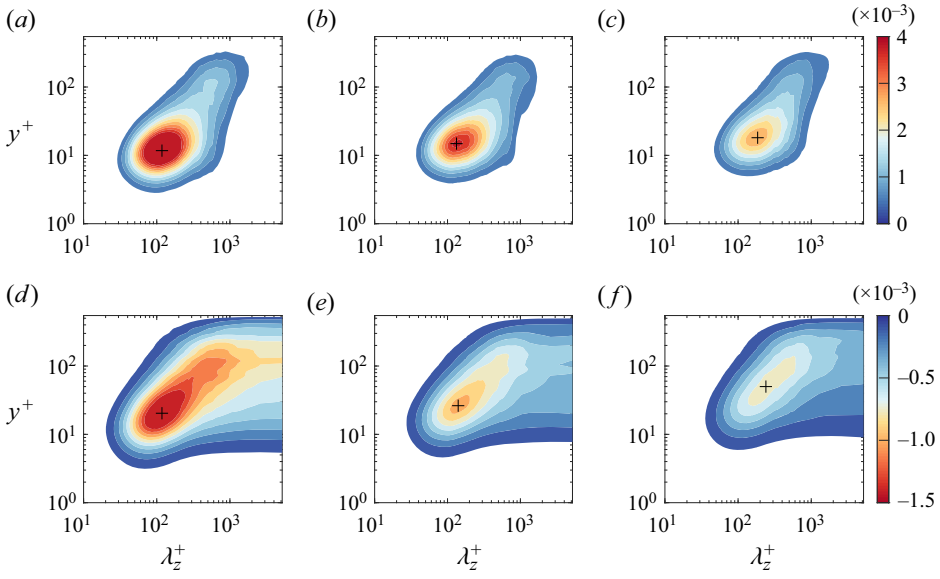

Figure 13. Spectral production contribution to the streamwise TKE budget $\hat{P}_{11}$ and Reynolds stress budget $\hat{P}_{12}$: (*a*) $\hat{P}_{11}$ for case C0, (*b*) $\hat{P}_{11}$ for case C1, (*c*) $\hat{P}_{11}$ for case C2, (*d*) $\hat{P}_{12}$ for case C0, (*e*) $\hat{P}_{12}$ for case C1, and (*f*) $\hat{P}_{12}$ for case C2. Here, $\hat{P}_{11}$ and $\hat{P}_{12}$ are normalized by u_τ^3/δ_ν. The plus signs (i.e. +) mark the peaks of the spectra.

To uncover the underlying physical mechanisms, we turn to evaluating the spectral production and feedback terms for the streamwise turbulent kinetic energy (TKE) and Reynolds stress budgets. Figure 13 displays the spectral production terms $\hat{P}_{11} = -\mathrm{Re}(\langle \hat{u}'(k_z, y)\, \hat{v}'^*(k_z, y)\rangle)\, \mathrm{d}\langle u\rangle/\mathrm{d}y$ for the streamwise TKE $\langle u'u'\rangle$ budget, and $\hat{P}_{12} = -\langle \hat{v}'(k_z, y)\, \hat{v}'^*(k_z, y)\rangle\, \mathrm{d}\langle u\rangle/\mathrm{d}y$ for the Reynolds stress $\langle u'v'\rangle$ budget, as a function of spanwise wavelength λ_z^+ and wall-normal location y^+. Here, $\mathrm{Re}(\cdot)$ represents the real part of a complex number. For all cases C0–C2, $\hat{P}_{11}$ is positive, whereas $\hat{P}_{12}$ is negative (because of $\langle u'v'\rangle < 0$) throughout the entire channel. The overall shapes of $\hat{P}_{11}$ resemble those of the premultiplied spectra $k_z\Phi_{uu}/u_\tau^2$. However, the patterns of $\hat{P}_{12}$ differ significantly from those of $\hat{P}_{11}$. For case C1, the magnitudes of both $\hat{P}_{11}$ and $\hat{P}_{12}$ are weakened, especially at the inner peaks (figures 13*b*,*e*). Again, this effect is more pronounced for case C2 (figures 13*c*,*f*), implying that inter-particle electrostatic forces suppress the production of $\langle u'u'\rangle$ and $\langle u'v'\rangle$ around the scales of LSMs. It is important to note that the same conclusions can be drawn for $\hat{P}_{11}$ and $\hat{P}_{12}$ as functions of the streamwise wavelength and wall-normal location, but they are not presented here and below for the sake of clarity.

Figure 14 shows the spectral feedback terms $\hat{\Psi}_{11} = \mathrm{Re}(\langle \widehat{F_x'}(k_z, y)\, \hat{u}'^*(k_z, y)\rangle)$ for the the streamwise TKE $\langle u'u'\rangle$ budget, and $\hat{\Psi}_{12} = \mathrm{Re}(\langle \widehat{F_x'}(k_z, y)\, \hat{v}'^*(k_z, y)\rangle + \langle \widehat{F_y'}(k_z, y)\, \hat{u}'^*(k_z, y)\rangle)$ for the Reynolds stress $\langle u'v'\rangle$ budget, where F_x' and F_y' denote the fluctuating particle feedback forces on the fluid phase in the streamwise and wall-normal directions, respectively. Interestingly, the spectral feedback terms $\hat{\Psi}_{11}$ and $\hat{\Psi}_{12}$ behave quite differently compared to the production terms. It is clear that for cases C1 and C2, $\hat{\Psi}_{11}$ is negative in the bulk of the channel, but positive within the viscous sublayer (i.e. $y^+ \lesssim 5$) at large spanwise

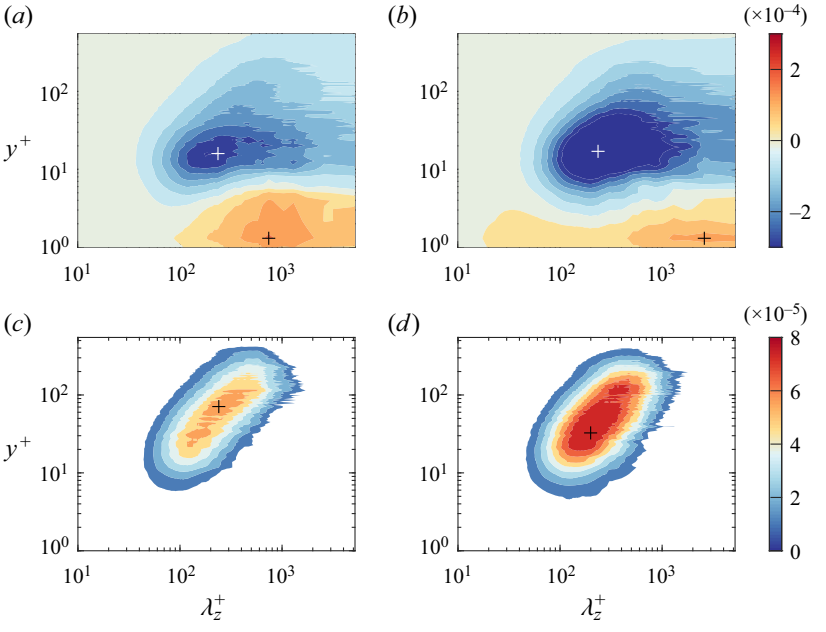

Figure 14. Spectral feedback term contribution to: (*a*) the streamwise TKE budget $\hat{\Psi}_{11}$ for case C1, (*b*) the streamwise TKE budget $\hat{\Psi}_{11}$ for case C2, (*c*) the Reynolds stress budget $\hat{\Psi}_{12}$ for case C1, and (*d*) the Reynolds stress budget $\hat{\Psi}_{12}$ for case C2. Here, $\hat{\Psi}_{11}$ and $\hat{\Psi}_{12}$ are normalized by u_τ^3/δ_ν. The plus signs (i.e. +) mark the peaks of the spectra.

wavelengths (figures 14*a*,*b*). The negative part of $\hat{\Psi}_{11}$ is peaked at $y^+ \approx 15$ and $\lambda_z^+ \approx 230$, while the positive part of $\hat{\Psi}_{11}$ is peaked at $y^+ \approx 1.5$ and $\lambda_z^+ \approx 750$. This bipolar behaviour is a result of the interplay between smaller ($St^+ = 25$) and larger ($St^+ = 120$) particles embedded in the fluid phase in cases C1 and C2 (see table 2). This is because Wang & Richter (2019*b*) have demonstrated that $\hat{\Psi}_{11}$ appears positive for the small-inertial particles ($St^+ = 2.4$–24.2), but negative for large-inertial particles ($St^+ = 60.5$–908). In contrast, $\hat{\Psi}_{12}$ is positive throughout the entire channel and is peaked at the same wavelength but at a relatively high wall-normal location, suggesting a different role for $\hat{\Psi}_{12}$ compared to $\hat{\Psi}_{11}$ (figures 14*c*,*d*). By comparing cases C1 and C2, we find that the negative part of $\hat{\Psi}_{11}$ and the whole of $\hat{\Psi}_{12}$ are both substantially enhanced when particles are charged, even though the positive part of $\hat{\Psi}_{11}$ shifts toward the wall and widens in the wavelength domain. This suggests that inter-particle electrostatic forces enhance the particle feedback around the scales of the LSMs, in accord with the enhancements of particle dissipation (see figure 10). Combining the results from figures 13 and 14, we can conclude that the attenuation of the intensity of LSMs by charged particles is caused by both reduction of turbulent production and enhancement of particle dissipation around the scales of LSMs by inter-particle electrostatic forces.

In contrast to premultiplied *u*-spectra, the two-point autocorrelation function of the fluctuating streamwise fluid velocity measures the average spatial fluid structure (Ganapathisubramani *et al.* 2005; Hutchins & Marusic 2007). Such autocorrelation functions in the streamwise–spanwise (*x*–*z*) and streamwise–wall-normal (*x*–*y*) planes,

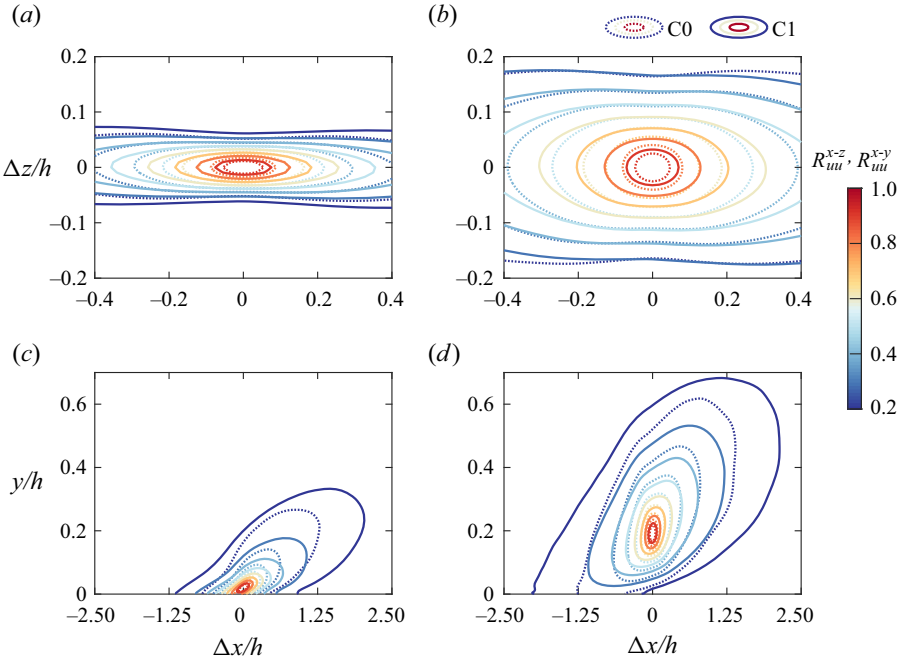

Figure 15. Two-point autocorrelation functions of the fluctuating streamwise fluid velocity: (*a*) in the *x*–*z* plane, R_{uu}^{x-z} with $y_{ref}/h = 1.95 \times 10^{-2}$ (equivalent to $y_{ref}/\delta_v = 10.5$); (*b*) in the *x*–*z* plane, R_{uu}^{x-z} with $y_{ref}/h = 0.19$ (equivalent to $y_{ref}/\delta_v = 103.1$); (*c*) in the *x*–*y* plane, R_{uu}^{x-y} with $y_{ref}/h = 1.95 \times 10^{-2}$; and (*d*) in the *x*–*y* plane, R_{uu}^{x-y} with $y_{ref}/h = 0.19$. Here, dotted and solid lines denote cases C0 and C1, respectively.

R_{uu}^{x-z} and R_{uu}^{x-y}, are respectively defined by

$$R_{uu}^{x-z}(\Delta x, \Delta z, y_{ref}) = \frac{\langle u'(x, z, y_{ref})\, u'(x + \Delta x, z + \Delta z, y_{ref})\rangle}{\langle u'^2(x, z, y_{ref})\rangle}, \tag{3.10}$$

$$R_{uu}^{x-y}(\Delta x, y, y_{ref}) = \frac{\langle u'(x, y_{ref}, z)\, u'(x + \Delta x, y, z)\rangle}{\langle u'^2(x, y_{ref}, z)\rangle^{1/2}\langle u'^2(x + \Delta x, y, z)\rangle^{1/2}}, \tag{3.11}$$

where y_{ref} is the reference wall-normal location at which the autocorrelation function is evaluated, and Δx and Δz are the in-plane streamwise and spanwise separations, respectively.

Figures 15 and 16 display comparisons of the autocorrelation functions between cases C0 and C1, and between C1 and C2, respectively. It can be seen that for all cases C0–C2, the autocorrelation function R_{uu}^{x-z} is highly elongated in the streamwise direction within the near-wall region (figures 15*a* and 16*a*), in line with the streaky structures observed in the instantaneous fluid velocity (figures 2*a*–*c*). However, these anisotropic streaky structures become longer and wider in the presence of uncharged particles (figure 15*a*), and this effect is more pronounced when the particles are charged (figure 16*a*), consistent with figures 2(*a*–*c*). This structural expansion can also be observed in the outer layer, but with relatively slight variations (figures 15*b* and 16*b*), which are caused by the disruptions of the self-sustaining near-wall cycle by larger particles, as discussed earlier.

Aside from R_{uu}^{x-z}, R_{uu}^{x-y} is also influenced by the presence of uncharged and charged particles. As shown in figures 15(*c*,*d*) and 16(*c*,*d*), the inclined structures of the fluid

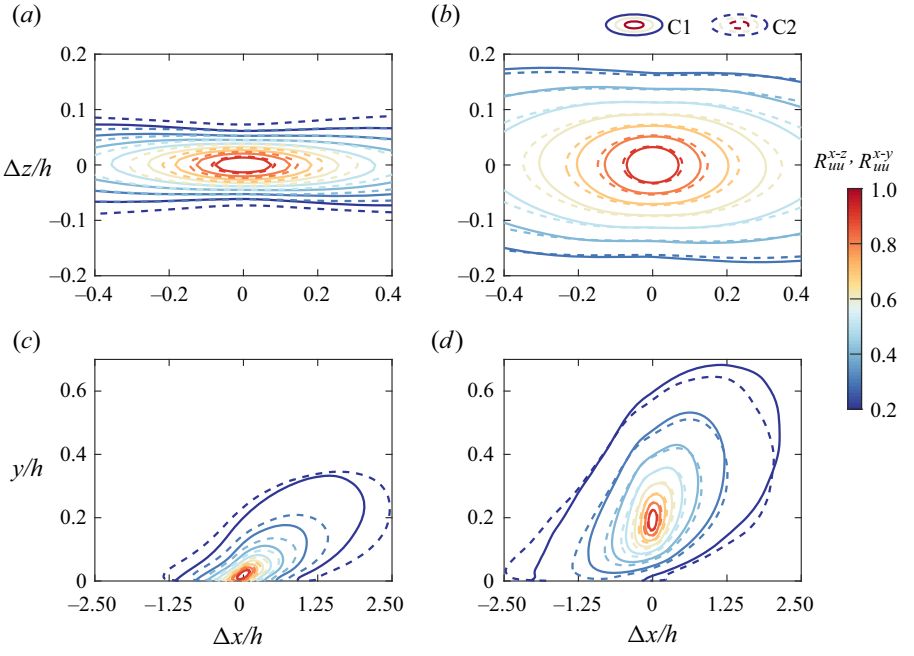

Figure 16. Same as figure 15, but for the comparisons of autocorrelation functions between cases C1 and C2, which are denoted by the solid and dashed lines, respectively.

velocity in the wall-normal planes become flatter due to the presence of particles, particularly in the case of flow laden with charged particles. The physical mechanisms responsible for this structural flattening are not yet fully understood. A possible explanation is that in the streamwise–wall-normal planes, particles form inclined rod-like clusters residing above the fluid structures (Zhu *et al.* 2021), which are expected to lower the downstream edge of the fluid structures towards the wall (Salesky & Anderson 2020). In summary, it appears that inter-particle electrostatic forces lead to the expansion of average streaky fluid structures in the streamwise–spanwise planes, and the flattening of average inclined fluid structures in the streamwise–wall-normal planes.

4. Conclusions

In this paper, utilizing point-particle direct numerical simulations, we investigate how charged bidisperse particles affect the turbulent intensity and structure of horizontal channel flows at friction Reynolds number $Re_\tau \approx 540$. A total of 3.2×10^7 bidisperse particles are released into the fluid flow, which is made up of two kinds of species, with equal amounts and mass density, but different diameters. The particle-to-fluid density ratio is set to match that of natural sand particles, i.e. $\rho_p/\rho_f = 2200$ (Zheng 2009). The diameter of the larger particles is 360 μm (0.99 in viscous units), and that of the smaller ones is 164 μm (0.45 in viscous units), corresponding to viscous Stokes numbers $St^+ = 25$ and 120, respectively. We consider three cases: an unladen flow (C0), a flow laden with uncharged particles (C1), and a flow laden with charged particles (C2). In case C2, the larger particles are positively charged, while the smaller ones are negatively charged, in accordance with the 'size-dependent' phenomena in particle electrification (Lacks &

Sankaran 2011; Zheng 2013). The main findings of the present study are summarized below.

Compared to case C0, the wall-normal profile of the inner-scaled mean streamwise fluid velocity is noticeably increased in the outer layer for case C1 due to a decrease in the fluid friction velocity. In contrast, the overall profile of the mean streamwise velocity is substantially shifted towards lower values. This opposite trend in the modulation of the inner-scaled mean streamwise fluid velocity for cases C1 and C2 can be explained by the substantial enhancement of particle mass loading below $y^+ \approx 180$ when particles are charged. It has been reported previously that particles with small and large mass loadings result in opposite effects on turbulence modulation (Li *et al.* 2001). As expected, turbulent intensity is inhibited by the presence of uncharged particles. However, in comparison to case C1, the root mean square streamwise, spanwise and wall-normal fluctuating velocities, as well as Reynolds stress for case C2, are remarkably diminished below $y^+ \approx 200$, with slight changes above $y^+ \approx 200$. This suggests that inter-particle electrostatic forces seem to further suppress turbulent intensities. The main reasons are twofold: the particle Reynolds numbers of the considered sub-Kolmogorov-sized particles are smaller than 5 and thus consistently suppress turbulent intensity, regardless of the presence of uncharged or charged particles; inter-particle electrostatic forces alter particle mass loading considerably in the near-wall region but negligibly in the outer region.

Even though viscous stress is found to be unaffected by the presence of uncharged and charged particles, turbulent Reynolds stress is significantly decreased, especially for case C2. Meanwhile, particle stress for case C1 is largely enhanced in case C2. This phenomenon indicates that inter-particle electrostatic forces promote the particles to extract momentum from the fluid phase. In particular, compared to case C1, although the contribution of turbulent Reynolds stress to the overall drag for case C2 is significantly reduced, due to a substantial increase in particle stress, the total overall drag for case C2 is further increased. Consequently, inter-particle electrostatic forces enhance the overall drag through an indirect mechanism: strengthening the contribution of the particle stress. Besides momentum exchange, inter-particle electrostatic forces also appear to facilitate kinetic energy transfer between particles and the fluid phase, leading to a considerable enhancement of extra dissipation by particles. Accordingly, the further reduction of turbulence intensity by charged particles results from enhanced momentum extraction and extra particle dissipation caused by inter-particle electrostatic forces.

The structural characteristics of the fluid phase are finally quantified by analysing premultiplied spectra and autocorrelation functions. It is shown that the large-scale motions (LSMs), corresponding to the inner peaks of the premultiplied spectra of streamwise fluid velocity, are shifted towards larger streamwise and spanwise scales, but their intensity is weakened in the presence of uncharged particles. These increases in length scale and decreases in intensity of LSMs are more pronounced when particles are charged. Based on the analysis of the spectral production and feedback terms for the streamwise turbulent kinetic energy and Reynolds stress budgets, we find that the attenuation of intensity of LSMs is due to the decrease in turbulent production and the increase in particle feedback around the scales of the LSMs by inter-particle electrostatic forces. Furthermore, the average spatial fluid structures are quantified using two-point autocorrelation functions. It is found that inter-particle electrostatic forces appear to expand the streaky fluid structures in the wall-parallel planes and flatten the inclined fluid structures in the wall-normal planes.

One limitation of this study is its focus solely on exploring the difference in turbulence modulation between uncharged particles and charged particles with a specific charge

level, at a given particle volume fraction. Future work warrants further investigation into exploring the quantitative laws and underlying physical mechanisms of particle-induced turbulence modulation, and even relaminarization, under different particle volume fractions and charges.

Funding. This work was supported by the National Natural Science Foundation of China (grant nos 12388101 and 92052202) and the Fundamental Research Funds for the Central Universities (grant no. lzujbky-2021-ey19).

Declaration of interests. The authors report no conflict of interest.

Author ORCIDs.
Huan Zhang https://orcid.org/0000-0001-8704-8688;
Xiaojing Zheng https://orcid.org/0000-0002-6845-2949.

Appendix A. Detailed derivation of the streamwise momentum balance equation for the fluid phase

On the basis of the momentum balance equation of the fluid phase (2.1), the mean momentum equation in the wall-normal direction is given by

$$0 = -\frac{\mathrm{d}\langle v'^2\rangle}{\mathrm{d}y} - \frac{1}{\rho_f}\frac{\partial\langle p\rangle}{\partial y} + \langle f_y\rangle. \tag{A1}$$

Integrating (A1) over the interval $[0, y]$, invoking boundary condition $\langle v'^2\rangle|_{y=0} = 0$, and taking the partial derivative with respect to x, we obtain

$$\frac{\partial\langle p\rangle}{\partial x} = \frac{\mathrm{d}p_w}{\mathrm{d}x}, \tag{A2}$$

where $p_w = \langle p(x, 0, 0)\rangle$ is the mean pressure on the bottom wall. Similarly, the mean momentum equation in the streamwise direction is

$$\frac{1}{\rho_f}\frac{\partial\langle p\rangle}{\partial x} = \frac{\partial}{\partial y}\left[\nu\frac{\partial\langle u\rangle}{\partial y} - \langle u'v'\rangle\right] + \langle f_x\rangle, \tag{A3}$$

which can be rewritten as

$$\frac{\mathrm{d}\tau_T}{\mathrm{d}y} = \frac{\partial\langle p\rangle}{\partial x}, \tag{A4}$$

with the total shear stress $\tau_T(y)$ defined by

$$\tau_T = \rho_f\nu\frac{\partial\langle u\rangle}{\partial y} - \rho_f\langle u'v'\rangle + \rho_f\int_h^y\langle f_x\rangle\,\mathrm{d}y. \tag{A5}$$

Combining (A2) and (A4), and mentioning that τ_T and p_w are functions of only y and x, respectively, these lead to

$$\frac{\mathrm{d}\tau_T}{\mathrm{d}y} = \frac{\mathrm{d}p_w}{\mathrm{d}x} = -\frac{\tau_w}{h}, \tag{A6}$$

where $\tau_w = \tau_T(0) = \rho_f(\partial\langle u\rangle/\partial y)|_{y=0} + \rho_f\int_h^0\langle f_x\rangle\,\mathrm{d}y$ denotes the wall shear stress. Integration of (A6) from 0 to y gives

$$\tau_T = \rho_f\nu\frac{\partial\langle u\rangle}{\partial y} - \rho_f\langle u'v'\rangle + \rho_f\int_h^y\langle f_x\rangle\,\mathrm{d}y = \tau_w\left(1 - \frac{y}{h}\right). \tag{A7}$$

Appendix B. Detailed derivation of the weighted integral presented in evaluating the contribution of different stresses to the overall drag

Combining (A2) and (A6), (A3) can be rewritten as

$$-\frac{\tau_w}{h} = \rho_f \langle f_x \rangle + \frac{\partial}{\partial y}\left[\rho_f \nu \frac{\partial \langle u \rangle}{\partial y} - \rho_f \langle u' v' \rangle\right]. \tag{B1}$$

Using the substitution $y^* = y/h$ and the corresponding relation

$$\frac{\partial}{\partial y} = \frac{\partial}{\partial y^*}\frac{\partial y^*}{\partial y} = \frac{1}{h}\frac{\partial}{\partial y^*}, \tag{B2}$$

we have

$$C_f = \frac{-2h\langle f_x \rangle}{U_b^2} - 2\frac{\partial}{\partial y^*}\left[\frac{1}{Re_b}\frac{\partial \langle u^* \rangle}{\partial y^*} - \langle u'^* v'^* \rangle\right], \tag{B3}$$

where $C_f = 2\tau_w/\rho_f U_b^2$ is the friction coefficient, $Re_b = U_b h/\nu$ is the bulk Reynolds number, $u'^* = u'/U_b$, and $v'^* = v'/U_b$. Applying triple integration $\int_0^1 \int_0^{y^*} \int_1^{y^*} \mathrm{d}y^* \, \mathrm{d}y^* \, \mathrm{d}y^*$ to (B3) and using the relations

$$\left(\frac{1}{Re_b}\frac{\partial \langle u^* \rangle}{\partial y^*} - \langle u'^* v'^* \rangle\right)\Big|_{y^*=1} = 0 \tag{B4}$$

and

$$\int_0^1 \int_0^{y^*} f(y^*)\, \mathrm{d}y^* \, \mathrm{d}y^* = \int_0^1 (1-y^*) f(y^*)\, \mathrm{d}y^*, \tag{B5}$$

we obtain

$$\begin{aligned} C_f = {} & \frac{6}{Re_b}\int_0^1 (1-y^*)\frac{\partial \langle u^* \rangle}{\partial y^*}\, \mathrm{d}y^* \\ & - 6\int_0^1 (1-y^*)\langle u'^* v'^* \rangle\, \mathrm{d}y^* \\ & + 6\int_0^1 (1-y^*)\left[\int_1^{y^*} \frac{h\langle f_x \rangle}{U_b^2}\, \mathrm{d}y^*\right] \mathrm{d}y^*. \end{aligned} \tag{B6}$$

For the triple integration, the first integration is believed to establish force balance. The second is considered to derive the mean velocity profile, while the third is accounted for obtaining the flow rate from the velocity (e.g. Fukagata, Iwamoto & Kasagi 2002; Yu *et al.* 2021). Again, using the substitution $y = hy^*$, (B6) can be rewritten as

$$\tau_w = \frac{1}{h}\left[\int_0^h 3\left(1-\frac{y}{h}\right)\tau_v\, \mathrm{d}y - \int_0^h 3\left(1-\frac{y}{h}\right)\tau_R\, \mathrm{d}y + \int_0^h 3\left(1-\frac{y}{h}\right)\tau_p\, \mathrm{d}y\right], \tag{B7}$$

where $\tau_v = \rho_f \nu(\partial\langle u \rangle/\partial y)$, $\tau_R = -\rho_f \langle u' v' \rangle$ and $\tau_p = \rho_f \int_h^y \langle f_x \rangle\, \mathrm{d}y$ are the fluid viscous, turbulent Reynolds and particle stresses, respectively. From (B7), it is clear that a weighted integral $\int_0^h 3(1-y/h)\, \mathrm{d}y$ should be considered in order to evaluate the contributions of different stresses to the wall shear stress. Notably, the weight function $1-y/h$ quantifies the differences in the contributions of stresses at various wall-normal positions to the wall shear stress.

References

Ahmed, A.M. & Elghobashi, S. 2000 On the mechanisms of modifying the structure of turbulent homogeneous shear flows by dispersed particles. *Phys. Fluids* **12**, 2906–2930.

Alipchenkov, V.M., Zaichik, L.I. & Petrov, O.F. 2004 Clustering of charged particles in isotropic turbulence. *High Temp.* **42**, 919–927.

Armenio, V. & Fiorotto, V. 2001 The importance of the forces acting on particles in turbulent flows. *Phys. Fluids* **13**, 2437–2440.

Balachandar, S. & Eaton, J.K. 2010 Turbulent dispersed multiphase flow. *Annu. Rev. Fluid Mech.* **42**, 111–133.

Boutsikakis, A., Fede, P. & Simonin, O. 2022 Effect of electrostatic forces on the dispersion of like-charged solid particles transported by homogeneous isotropic turbulence. *J. Fluid Mech.* **938**, A33.

Brandt, L. & Coletti, F. 2022 Particle-laden turbulence: progress and perspectives. *Annu. Rev. Fluid Mech.* **54**, 159–189.

Capecelatro, J. & Desjardins, O. 2013 An Euler–Lagrange strategy for simulating particle-laden flows. *J. Comput. Phys.* **238**, 1–31.

Capecelatro, J., Desjardins, O. & Fox, R.O. 2014 Numerical study of collisional particle dynamics in cluster-induced turbulence. *J. Fluid Mech.* **747**, R2.

Capecelatro, J., Desjardins, O. & Fox, R.O. 2015 On fluid–particle dynamics in fully developed cluster-induced turbulence. *J. Fluid Mech.* **780**, 578–635.

Caporaloni, M., Tampieri, F., Trombetti, F. & Vittori, O. 1975 Transfer of particles in nonisotropic air turbulence. *J. Aerosol Sci.* **32**, 565–568.

Chan, L., MacDonald, M., Chung, D., Hutchins, N. & Ooi, A. 2015 A systematic investigation of roughness height and wavelength in turbulent pipe flow in the transitionally rough regime. *J. Fluid Mech.* **771**, 743–777.

Costa, P. 2018 A FFT-based finite-difference solver for massively-parallel direct numerical simulations of turbulent flows. *Comput. Maths Applics* **76**, 1853–1862.

Costa, P., Brandt, L. & Picano, F. 2020 Interface-resolved simulations of small inertial particles in turbulent channel flow. *J. Fluid Mech.* **883**, A54.

Costa, P., Brandt, L. & Picano, F. 2021 Near-wall turbulence modulation by small inertial particles. *J. Fluid Mech.* **922**, A9.

Dave, H. & Kasbaoui, M.H. 2023 Mechanisms of drag reduction by semidilute inertial particles in turbulent channel flow. *Phys. Rev. Fluids* **8**, 084305.

Del Alamo, J.C. & Jiménez, J. 2003 Spectra of the very large anisotropic scales in turbulent channels. *Phys. Fluids* **15**, L41–L44.

Dhariwal, R. & Bragg, A.D. 2018 Small-scale dynamics of settling, bidisperse particles in turbulence. *J. Fluid Mech.* **839**, 594–620.

Di Renzo, M. & Urzay, J. 2018 Aerodynamic generation of electric fields in turbulence laden with charged inertial particles. *Nat. Commun.* **9**, 1676.

Dritselis, C.D. & Vlachos, N.S. 2008 Numerical study of educed coherent structures in the near-wall region of a particle-laden channel flow. *Phys. Fluids* **20**, 055103.

Duan, Y., Chen, Q., Li, D. & Zhong, Q. 2020 Contributions of very large-scale motions to turbulence statistics in open channel flows. *J. Fluid Mech.* **892**, A3.

Eaton, J.K. & Fessler, J. 1994 Preferential concentration of particles by turbulence. *Intl J. Multiphase Flow* **20**, 169–209.

Elghobashi, S. 1994 On predicting particle-laden turbulent flows. *Appl. Sci. Res.* **52**, 309–329.

Esmaily, M. & Horwitz, J. 2018 A correction scheme for two-way coupled point-particle simulations on anisotropic grids. *J. Comput. Phys.* **375**, 960–982.

Fong, K.O., Amili, O. & Coletti, F. 2019 Velocity and spatial distribution of inertial particles in a turbulent channel flow. *J. Fluid Mech.* **872**, 367–406.

Fukagata, K., Iwamoto, K. & Kasagi, N. 2002 Contribution of Reynolds stress distribution to the skin friction in wall-bounded flows. *Phys. Fluids* **14**, L73–L76.

Ganapathisubramani, B., Hutchins, N., Hambleton, W.T., Longmire, E.K. & Marusic, I. 2005 Investigation of large-scale coherence in a turbulent boundary layer using two-point correlations. *J. Fluid Mech.* **524**, 57–80.

Gao, W., Samtaney, R. & Richter, D.H. 2023 Direct numerical simulation of particle-laden flow in an open channel at $Re_\tau = 5186$. *J. Fluid Mech.* **957**, A3.

Garcia-Mayoral, R. & Jiménez, J. 2011 Hydrodynamic stability and breakdown of the viscous regime over riblets. *J. Fluid Mech.* **678**, 317–347.

GORE, R.A. & CROWE, C.T. 1989 Effect of particle size on modulating turbulent intensity. *Intl J. Multiphase Flow* **15**, 279–285.

GORE, R.A. & CROWE, C.T. 1991 Modulation of turbulence by a dispersed phase. *Trans. ASME J. Fluids Engng* **113**, 304–307.

GROSSHANS, H., BISSINGER, C., CALERO, M. & PAPALEXANDRIS, M.V. 2021 The effect of electrostatic charges on particle-laden duct flows. *J. Fluid Mech.* **909**, A21.

GROSSHANS, H. & PAPALEXANDRIS, M.V. 2016 Large eddy simulation of triboelectric charging in pneumatic powder transport. *Powder Technol.* **301**, 1008–1015.

GROSSHANS, H. & PAPALEXANDRIS, M.V. 2017 Direct numerical simulation of triboelectric charging in particle-laden turbulent channel flows. *J. Fluid Mech.* **818**, 465–491.

GUALA, M., HOMMEMA, S.E. & ADRIAN, R.J. 2006 Large-scale and very-large-scale motions in turbulent pipe flow. *J. Fluid Mech.* **554**, 521–542.

GUALTIERI, P., PICANO, F., SARDINA, G. & CASCIOLA, C. 2013 Clustering and turbulence modulation in particle-laden shear flows. *J. Fluid Mech.* **715**, 134–162.

HAMAMOTO, N., NAKAJIMA, Y. & SATO, T. 1992 Experimental discussion on maximum surface charge density of fine particles sustainable in normal atmosphere. *J. Electrost.* **28**, 161–173.

HETSRONI, G. 1989 Particles–turbulence interaction. *Intl J. Multiphase Flow* **15**, 735–746.

HORWITZ, J.A.K. & MANI, A. 2016 Accurate calculation of Stokes drag for point-particle tracking in two-way coupled flows. *J. Comput. Phys.* **318**, 85–109.

HUTCHINS, N. & MARUSIC, I. 2007 Evidence of very long meandering features in the logarithmic region of turbulent boundary layers. *J. Fluid Mech.* **579**, 1–28.

HWANG, W. & EATON, J.K. 2006 Homogeneous and isotropic turbulence modulation by small heavy ($St \sim 50$) particles. *J. Fluid Mech.* **564**, 361–393.

JIE, Y., CUI, Z., XU, C. & ZHAO, L. 2022 On the existence and formation of multi-scale particle streaks in turbulent channel flows. *J. Fluid Mech.* **935**, A18.

JIMÉNEZ, J. & PINELLI, A. 1999 The autonomous cycle of near-wall turbulence. *J. Fluid Mech.* **389**, 335–359.

JOHNSON, P.L., BASSENNE, M. & MOIN, P. 2020 Turbophoresis of small inertial particles: theoretical considerations and application to wall-modelled large-eddy simulations. *J. Fluid Mech.* **883**, A27.

JOHNSON, T.A. & PATEL, V.C. 1999 Flow past a sphere up to a Reynolds number of 300. *J. Fluid Mech.* **378**, 19–70.

KAFTORI, D., HETSRONI, G. & BANERJEE, S. 1998 The effect of particles on wall turbulence. *Intl J. Multiphase Flow* **24**, 359–386.

KARNIK, A.U. & SHRIMPTON, J.S. 2012 Mitigation of preferential concentration of small inertial particles in stationary isotropic turbulence using electrical and gravitational body forces. *Phys. Fluids* **24**, 073301.

KASBAOUI, M.H. 2019 Turbulence modulation by settling inertial aerosols in Eulerian–Eulerian and Eulerian–Lagrangian simulations of homogeneously sheared turbulence. *Phys. Rev. Fluids* **4**, 124308.

KIM, J. & MOIN, P. 1985 Application of a fractional-step method to incompressible Navier–Stokes equations. *J. Comput. Phys.* **59**, 308–323.

KOLEHMAINEN, J., OZEL, A., BOYCE, C.M. & SUNDARESAN, S. 2016 A hybrid approach to computing electrostatic forces in fluidized beds of charged particles. *AICHE J.* **62**, 2282–2295.

KULICK, J.D., FESSLER, J.R. & EATON, J.K. 1994 Particle response and turbulence modification in fully developed channel flow. *J. Fluid Mech.* **277**, 109–134.

KUSSIN, J. & SOMMERFELD, M. 2002 Experimental studies on particle behaviour and turbulence modification in horizontal channel flow with different wall roughness. *Exp. Fluids* **33**, 143–159.

LACKS, D.J. & SANKARAN, R.M. 2011 Contact electrification of insulating materials. *J. Phys.* D*: Appl. Phys.* **44**, 453001.

LAVRINENKO, A., FABREGAT, A. & PALLARES, J. 2022 Comparison between fully resolved and time-averaged simulations of particle cloud dispersion produced by a violent expiratory event. *Acta Mechanica Sin.* **38**, 721489.

LEE, J. & LEE, C. 2015 Modification of particle-laden near-wall turbulence: effect of Stokes number. *Phys. Fluids* **27**, 023303.

LEE, M. & MOSER, R.D. 2015 Direct numerical simulation of turbulent channel flow up to $Re_\tau \approx 5200$. *J. Fluid Mech.* **774**, 395–415.

LI, D., LUO, K. & FAN, J. 2016 Modulation of turbulence by dispersed solid particles in a spatially developing flat-plate boundary layer. *J. Fluid Mech.* **802**, 359–394.

LI, J., WANG, H., LIU, Z., CHEN, S. & ZHENG, C. 2012 An experimental study on turbulence modification in the near-wall boundary layer of a dilute gas–particle channel flow. *Exp. Fluids* **53**, 1385–1403.

LI, Y., MCLAUGHLIN, J.B., KONTOMARIS, K. & PORTELA, L. 2001 Numerical simulation of particle-laden turbulent channel flow. *Phys. Fluids* **13**, 2957–2967.

LU, J., NORDSIEK, H., SAW, E.W. & SHAW, R.A. 2010 Clustering of charged inertial particles in turbulence. *Phys. Rev. Lett.* **104**, 184505.

LU, J. & SHAW, R.A. 2015 Charged particle dynamics in turbulence: theory and direct numerical simulations. *Phys. Fluids* **27**, 065111.

MARCHIOLI, C. & SOLDATI, A. 2002 Mechanisms for particle transfer and segregation in a turbulent boundary layer. *J. Fluid Mech.* **468**, 283–315.

MAXEY, M.R. 1987 The gravitational settling of aerosol particles in homogeneous turbulence and random flow fields. *J. Fluid Mech.* **174**, 441–465.

MAXEY, M.R. & RILEY, J.J. 1983 Equation of motion for a small rigid sphere in a nonuniform flow. *Phys. Fluids* **26**, 883–889.

MOTOORI, Y., WONG, C. & GOTO, S. 2022 Role of the hierarchy of coherent structures in the transport of heavy small particles in turbulent channel flow. *J. Fluid Mech.* **942**, A3.

MURAMULLA, P., TYAGI, A., GOSWAMI, P.S. & KUMARAN, V. 2020 Disruption of turbulence due to particle loading in a dilute gas–particle suspension. *J. Fluid Mech.* **889**, A28.

OWEN, P.R. 1969 Pneumatic transport. *J. Fluid Mech.* **39**, 407–432.

PAN, Y. & BANERJEE, S. 1996 Numerical simulation of particle interactions with wall turbulence. *Phys. Fluids* **8**, 2733–2755.

PAN, Y. & BANERJEE, S. 1997 Numerical investigation of the effects of large particles on wall-turbulence. *Phys. Fluids* **9**, 3786–3807.

PENG, C., AYALA, O.M. & WANG, L.P. 2019 A direct numerical investigation of two-way interactions in a particle-laden turbulent channel flow. *J. Fluid Mech.* **875**, 1096–1144.

PICANO, F., BREUGEM, W.P. & BRANDT, L. 2015 Turbulent channel flow of dense suspensions of neutrally buoyant spheres. *J. Fluid Mech.* **764**, 463–487.

POPE, S.B. 2000 *Turbulent Flows*. Cambridge University Press.

REEKS, M.W. 1983 The transport of discrete particles in inhomogeneous turbulence. *J. Aerosol Sci.* **14**, 729–739.

RICHTER, D.H. & SULLIVAN, P.P. 2013 Momentum transfer in a turbulent, particle-laden Couette flow. *Phys. Fluids* **25**, 053304.

RICHTER, D.H. & SULLIVAN, P.P. 2014 Modification of near-wall coherent structures by inertial particles. *Phys. Fluids* **26**, 103304.

RUAN, X., GORMAN, M.T. & NI, R. 2024 Effects of electrostatic interaction on clustering and collision of bidispersed inertial particles in homogeneous and isotropic turbulence. *J. Fluid Mech.* **980**, A29.

SALESKY, S.T. & ANDERSON, W. 2020 Revisiting inclination of large-scale motions in unstably stratified channel flow. *J. Fluid Mech.* **884**, R5.

SARDINA, G., SCHLATTER, P., BRANDT, L., PICANO, F. & CASCIOLA, C.M. 2012 Wall accumulation and spatial localization in particle-laden wall flows. *J. Fluid Mech.* **699**, 50–78.

SCHILLER, L. & NAUMANN, A. 1935 A drag coefficient correlation. *Z. Verein. Deutsch. Ing.* **77**, 318–320.

SCHOPPA, W. & HUSSAIN, F. 2002 Coherent structure generation in near-wall turbulence. *J. Fluid Mech.* **453**, 57–108.

SCHUMANN, U. & SWEET, R.A. 1988 Fast Fourier transforms for direct solution of Poisson's equation with staggered boundary conditions. *J. Comput. Phys.* **75**, 123–137.

SCHWINDT, N., VON PIDOLL, U., MARKUS, D., KLAUSMEYER, U., PAPALEXANDRIS, M.V. & GROSSHANS, H. 2017 Measurement of electrostatic charging during pneumatic conveying of powders. *J. Loss Prev. Process Ind.* **49**, 461–471.

SHAO, X., WU, T. & YU, Z. 2012 Fully resolved numerical simulation of particle-laden turbulent flow in a horizontal channel at a low Reynolds number. *J. Fluid Mech.* **693**, 319–344.

SIPPOLA, P., KOLEHMAINEN, J., OZEL, A., LIU, X., SAARENRINNE, P. & SUNDARESAN, S. 2018 Experimental and numerical study of wall layer development in a tribocharged fluidized bed. *J. Fluid Mech.* **849**, 860–884.

SQUIRES, K.D. & EATON, J.K. 1990 Particle response and turbulence modification in isotropic turbulence. *Phys. Fluids A: Fluid Dyn.* **2**, 1191–1203.

TOUBER, E. & LESCHZINER, M.A. 2012 Near-wall streak modification by spanwise oscillatory wall motion and drag-reduction mechanisms. *J. Fluid Mech.* **693**, 150–200.

TSUJI, Y. & MORIKAWA, Y. 1982 LDV measurements of an air–solid two-phase flow in a horizontal pipe. *J. Fluid Mech.* **120**, 385–409.

TSUJI, Y., MORIKAWA, Y. & SHIOMI, H. 1984 LDV measurements of an air–solid two-phase flow in a vertical pipe. *J. Fluid Mech.* **139**, 417–434.

VANCE, M.W., SQUIRES, K.D. & SIMONIN, O. 2006 Properties of the particle velocity field in gas–solid turbulent channel flow. *Phys. Fluids* **18**, 063302.

VREMAN, A. 2015 Turbulence attenuation in particle-laden flow in smooth and rough channels. *J. Fluid Mech.* **773**, 103–136.

WANG, G. & RICHTER, D.H. 2019*a* Modulation of the turbulence regeneration cycle by inertial particles in planar Couette flow. *J. Fluid Mech.* **861**, 901–929.

WANG, G. & RICHTER, D.H. 2019*b* Two mechanisms of modulation of very-large-scale motions by inertial particles in open channel flow. *J. Fluid Mech.* **868**, 538–559.

WANG, G. & ZHENG, X. 2016 Very large scale motions in the atmospheric surface layer: a field investigation. *J. Fluid Mech.* **802**, 464–489.

WANG, L.P., WEXLER, A.S. & ZHOU, Y. 2000 Statistical mechanical description and modelling of turbulent collision of inertial particles. *J. Fluid Mech.* **415**, 117–153.

YAO, J., CHEN, X. & HUSSAIN, F. 2022 Direct numerical simulation of turbulent open channel flows at moderately high Reynolds numbers. *J. Fluid Mech.* **953**, A19.

YOUSEFI, A., COSTA, P., PICANO, F. & BRANDT, L. 2023 On the role of inertia in channel flows of finite-size neutrally buoyant particles. *J. Fluid Mech.* **955**, A30.

YU, Z., XIA, Y., GUO, Y. & LIN, J. 2021 Modulation of turbulence intensity by heavy finite-size particles in upward channel flow. *J. Fluid Mech.* **913**, A3.

ZHANG, H., CUI, Y. & ZHENG, X. 2023*a* How electrostatic forces affect particle behaviour in turbulent channel flows. *J. Fluid Mech.* **967**, A8.

ZHANG, H., TAN, X. & ZHENG, X. 2023*b* Multifield intermittency of dust storm turbulence in the atmospheric surface layer. *J. Fluid Mech.* **963**, A15.

ZHANG, H. & ZHOU, Y.H. 2020 Reconstructing the electrical structure of dust storms from locally observed electric field data. *Nat. Commun.* **11**, 5072.

ZHANG, H. & ZHOU, Y.H. 2023 Unveiling the spectrum of electrohydrodynamic turbulence in dust storms. *Nat. Commun.* **14**, 408.

ZHAO, L., ANDERSSON, H.I. & GILLISSEN, J.J. 2013 Interphasial energy transfer and particle dissipation in particle-laden wall turbulence. *J. Fluid Mech.* **715**, 32–59.

ZHAO, L.H., ANDERSSON, H.I. & GILLISSEN, J.J.J. 2010 Turbulence modulation and drag reduction by spherical particles. *Phys. Fluids* **22**, 081702.

ZHENG, X. 2009 *Mechanics of Wind-blown Sand Movements*. Springer Science & Business Media.

ZHENG, X., FENG, S. & WANG, P. 2021 Modulation of turbulence by saltating particles on erodible bed surface. *J. Fluid Mech.* **918**, A16.

ZHENG, X.J. 2013 Electrification of wind-blown sand: recent advances and key issues. *Eur. Phys. J.* E **36**, 138.

ZHENG, X.J., HUANG, N. & ZHOU, Y.H. 2003 Laboratory measurement of electrification of wind-blown sands and simulation of its effect on sand saltation movement. *J. Geophys. Res.* **108**, 4322.

ZHENG, X.J., HUANG, N. & ZHOU, Y.H. 2006 The effect of electrostatic force on the evolution of sand saltation cloud. *Eur. Phys. J.* E **19**, 129–138.

ZHOU, Y., WEXLER, A.S. & WANG, L.P. 2001 Modelling turbulent collision of bidisperse inertial particles. *J. Fluid Mech.* **433**, 77–104.

ZHU, H., PAN, C., WANG, G., LIANG, Y., JI, X. & WANG, J. 2021 Attached eddy-like particle clustering in a turbulent boundary layer under net sedimentation conditions. *J. Fluid Mech.* **920**, A53.